JOURNAL OF GEOPHYSICAL RESEARCH, VOL. 102, NO. C6, PAGES 12,609-12,646, JUNE 15, 1997

Sensitivity of a global sea ice model to the treatment of ice thermodynamics and dynamics

T. Fichefet and M. A. Morales Maqueda [1]

Institut d'Astronomie et de Géophysique G. Lemaître, Université Catholique de Louvain, Louvain-la-Neuve, Belgium

Abstract. The sensitivity of a global thermodynamic-dynamic sea ice model coupled to a one-dimensional upper ocean model to degradations of the model physics is investigated. The thermodynamic component of the sea ice model takes into consideration the presence of snow on top of sea ice, the storage of sensible and latent heat inside the snow-ice system, the influence of the subgrid-scale snow and ice thickness distributions on sea ice thermodynamics, the transformation of snow into snow ice when snow depth increases to the point where the snow-ice interface sinks below the waterline, and the existence of leads and polynyas (areas of open water) within the ice cover. Ice dynamics is treated basically as by *Hibler* [1979]. Regarding the upper ocean model, it is made up of an integral mixed layer model and of a diffusive model of the pycnocline. Advection of heat and salt by oceanic currents is implicitly accounted for by restoring the temperatures and salinities of the water column to annual mean data. It is very important to note that a single set of parameter values is employed to simultaneously simulate the Arctic and Antarctic ice regimes. A control run carried out with the model demonstrates that it does reasonably well in simulating the seasonal waxing and waning of both ice packs. The sensitivity study focuses on physical processes pertaining to (1) the vertical growth and decay of sea ice (thermal inertia of snow and ice, heat conduction, and snow cover), (2) the lateral growth and decay of sea ice (leads and polynyas), and (3) the sea ice dynamics (ice motion and shear strength). A total of nine sensitivity experiments have been performed. Each experiment consisted of removing a particular parameterization from the control run computer code. It appears that the thermal inertia of the snow-ice system is negligible in the Antarctic but not in the Arctic, where the total heat content of sea ice is chiefly dictated by internal storage of latent heat in brine pockets, sensible heat storage being of very minor consequence. It is also found that the inclusion of a prognostic snow layer and of a scheme of snow ice formation is important for sea ice modeling in the southern hemisphere. Furthermore, our results suggest that the thermodynamic effect of the subgrid-scale snow and ice thickness distributions, the existence of open water areas within the ice cover, and the ice motion play a crucial role in determining the seasonal behavior of both ice packs. The ice shear strength seems to be of lesser importance, although it has a nonnegligible effect in both hemispheres. We can therefore conclude that all these processes should be represented in global climate models.

1. Introduction

At high latitudes, the interactions between atmosphere and ocean are profoundly modified by the presence of sea ice. Sea ice represents an obstacle to air-sea exchanges of heat, mass, and momentum, and it is also an agent that reshapes their seasonal cycle. The role of sea ice as obstacle derives from its peculiar radiative, thermal, and mechanical properties. As a result of its high albedo and of its low thermal conductivity and porosity, sea ice dramatically affects the radiative as well as the turbulent components of the surface heat balance, cutting the absorption of shortwave radiation down to less than 20% in the case of snow-covered ice and reducing the sensible and latent heat fluxes by as much as 2 orders of magnitude. The sea ice cover also intercepts a large portion of the falling snow and prevents it from immediately contributing to the freshwater

[1]Now at Department of Mathematics, Keele University, Staffordshire, England.

Paper number 97JC00480.
0148-0227/97/97JC-00480$09.00

balance of the ocean. Finally, because of its strong resistance to convergent motion, a thick and compact ice pack hinders the free transfer of momentum from the atmosphere to the ocean. The role of sea ice as reshaping agent is related to the heat and salt fluxes involved in the processes of freezing and thawing. The freezing of seawater and the melting of sea ice are accompanied by a release and an absorption of latent heat, respectively, that delay the seasonal temperature extremes. By the destabilizing effect due to salt rejection during freezing and the contrary stabilizing effect due to the influx of low-salinity water into the water column during ice melting, the cyclic appearance and disappearance of sea ice tend to alter the baroclinic structure of the ocean and hence its thermohaline circulation. The coupling of the ice drift to the aforementioned processes adds further complexity to the picture. On the one hand, the differential motion of the ice is responsible both for the presence of leads and polynyas (areas of open water) within the ice cover and for the existence of ice ridges, structures that substantially change the local surface fluxes. On the other hand, the ice drift combines with the ice production and destruction to bring about, on an annual average, a net poleward transport of thermal energy in the atmosphere and of salt in the ocean. (For a more detailed discussion of the role of sea ice in the polar regions, see, for example, *The Polar Group* [1980].)

While the claim that sea ice plays a key role in shaping the climate at local-to-regional scales in the polar regions seems to be solidly substantiated, the extension of this claim to the global scale rests on less sound foundations so far. It is conjectured that a certain number of positive and negative feedback mechanisms relating sea ice to surface albedo, cloud cover, and atmospheric water vapor content could take an important part in determining the Earth's climate and its sensitivity to perturbations of natural or human origin. In default of global and comprehensive observations of the climate system, the only way presently at hand to assess the effective reach of the influence of sea ice upon climate seems to be the use of coupled atmosphere-ocean general circulation models (AOGCMs) incorporating detailed enough representations of sea ice. Unfortunately, results from modeling studies in which AOGCMs are employed to specifically investigate the back and forth interactions between sea ice and climate are, to the best of our knowledge, not yet available.

This state of affairs has relatively troubling implications with regard to the present very active research on the potential climatic warming induced by anthropogenic emissions of greenhouse gases. The numerical simulations motivated by this problem exhibit an enhanced climate response at high latitudes, especially in the northern hemisphere. Basically, this is thought to be due to the strong stability of the polar atmosphere and to positive feedbacks between sea ice and surface fluxes, among which the ice-albedo feedback is perhaps the most certain [*Curry et al.*, 1995]. However, the treatment of sea ice in the models used for these experiments is rather crude and the suspicion that the absence of some relevant sea ice mechanisms could introduce significant biases in their accentuated response over the polar regions is hard to avoid.

Let us focus on the current most advanced modeling studies of greenhouse–gas–induced climatic change, i.e., those simulating with AOGCMs the transient response of climate to the gradual increase in greenhouse gas concentrations (see *Manabe et al.* [1991], *Cubasch et al.* [1992], *Meehl et al.* [1993], and *Murphy and Mitchell* [1995]; hereinafter referred to as MAAL, CAL, MEAL, and MM, respectively). These studies predict an annual mean surface warming for the end of the next century that lies between 3°C and 7°C north of 65°N. Among the sea ice properties and processes that could possibly affect the results of these experiments and that are insufficiently treated in all or some of them, the following six should be underlined: (1) the strong dependence of the snow and ice albedos on surface conditions (CAL, MEAL, and MM use parameterizations that relate albedo to surface temperature alone, while MAAL also take into account the effect of ice thickness; (2) the thermal inertia of the snow-ice system and, in particular, the buffering effect associated with the volume changes in the internal brine pockets (absent from the four models); (3) the distribution of sea ice in different thickness categories within a given oceanic area, which greatly affects the local average thermodynamic growth rate of the ice (absent from the four models); (4) the presence of a snow cover on top of sea ice (ignored by MAAL and CAL) and the transformation of snow into ice due to flooding of the ice floes (ignored by MAAL, CAL, and MEAL); (5) the existence of a variable fraction of leads and polynyas within the pack (ignored by MAAL, CAL, and MEAL); and (6) the dynamics of sea ice (ignored by MEAL and MM, while MAAL and CAL employ simplistic schemes). Regarding this last point, a recent work by *Pollard and Thompson* [1994] suggests that ice motion might play a significant role in moderating the climate response to an increase in greenhouse gas amounts.

There is an urgent need for studies aiming to identify those aspects of the sea ice physics that have to be included in global coupled models in order to obtain more reliable simulations of climate. These studies should naturally be carried out with AOGCMs coupled to comprehensive thermodynamic-dynamic sea ice models. Hitherto, modelers have been prevented from embarking on this kind of investigations because of the considerable amount of computing time they would require. It is only recently that AOGCMs have started incorporating more elaborate sea ice formulations than those contained in the models cited above [e.g., *Lunkeit et al.*, 1996]. However, sensitivity studies on the interplay between sea ice and climate with these AOGCMs have not yet been published. Waiting for simulations of this type, experiments with uncoupled sea ice models represent very useful exercises that can shed, in the meantime, some light on the matter. In a sort of zero-order approximation, these experiments allow the quan-

tification of the influence of various sea ice processes on the modeled behavior of sea ice itself. As a matter of fact, if the uncoupled sea ice model appears sensitive to a perturbation in a particular parameterization, one can expect with good reason that the perturbation will also produce a significant response when the ice model will be introduced into an AOGCM.

There is already a fair, if not large number of sensitivity studies performed with stand-alone sea ice models or with coupled ice-ocean models (we shall have the opportunity to refer to them later on). However, a major limitation of these investigations is that all of them have been restricted to one or other of the hemispheric ice covers. In view of the pronounced differences between the Arctic and Antarctic environments, it is not clear that results obtained for one of the ice packs are of immediate application to the other. Trying to fill, in some manner, this gap, we present here a sensitivity study with a global sea ice model. More precisely, we examine the impact on the model performance of the simplifications currently made in climate models, with the exception of those related to sea ice albedo, whose study we leave for a forthcoming paper.

Our sea ice model incorporates parameterizations of the most relevant thermodynamic and dynamic sea ice processes. It is coupled to a one-dimensional upper ocean model that determines the depth, temperature, and salinity of the mixed layer and the temperature and salinity profiles in the pycnocline. In order to keep the model solution from developing long-term biases, the temperature and salinity are relaxed toward climatology at all oceanic levels. At the surface, this ice-ocean model is driven by atmospheric fluxes derived from climatological data fields. The model forcing also includes climatological surface geostrophic ocean currents. It is worth stressing that any feedback between atmosphere, sea ice, and ocean dynamics is ignored. Caution must therefore be exercised when drawing conclusions from the sensitivity experiments presented here. On the other hand, our purpose in the present work is to focus our attention on the response of sea ice. So, little attention will be paid to the oceanic processes and the sensitivity of oceanic variables, with exception made of the water-ice exchange of sensible heat. Within the scope of this study, the ocean model serves no other purpose than that of providing the required spatiotemporal variability of this heat flux.

Another point that deserves to be mentioned here is that we have attached ourselves to the principle of employing a single set of parameter values to simultaneously simulate the Arctic and Antarctic ice covers. Such a policy appears to us as an indispensable requisite both for a meaningful validation of the global model and for a reliable analysis of its sensitivity. A hemispheric tuning of the snow and ice parameters would allow one to optimize the realism of the simulation at the price of making difficult, if not impossible, a sound intercomparison of the modeled Arctic and Antarctic ice regimes.

The rest of the paper is organized as follows. Section 2 provides a detailed description of the model. A control simulation of the seasonal cycle of the Arctic and Antarctic ice packs is examined in section 3. Section 4 is devoted to the presentation and discussion of the sensitivity experiments. A summary and some concluding remarks are given in section 5.

2. Description of the Model

The model used in this work is based on the sea ice–upper ocean model of *Fichefet and Gaspar* [1988], the new features being that it is now defined on a global domain and that it incorporates a detailed representation of ice dynamics and a more complete treatment of the thermodynamic processes affecting sea ice. The various components of the model and the way in which they are coupled together are presented here. This section also deals with the numerical techniques employed to solve the model equations, with the configuration of the model grid, and with the forcing.

2.1. Sea Ice Model

The sea ice model takes into account the heat capacity of the snow-ice system, the effect of the subgrid-scale snow and ice thickness distributions on sea ice thermodynamics, the storage of latent heat in the brine pockets trapped inside the ice, and the formation of snow ice under excessive snow loading. It also allows for the presence of leads and polynyas within the ice cover. Ice dynamics is computed by assuming that sea ice behaves as a two-dimensional viscous-plastic continuum.

2.1.1. Vertical growth and decay of the ice. The model component that determines the vertical growth and decay of the ice due to thermodynamic processes is essentially an improved version of *Semtner*'s [1976] three-layer model. Within the ice-covered portion of each grid cell, sea ice is supposed to be a horizontally homogeneous slab of ice (divided into two layers of equal thickness) on which snow may accumulate when the surface temperature is below the melting point.

Internal temperatures of snow and ice are governed by a one-dimensional heat diffusion equation,

$$\rho c_p \frac{\partial T}{\partial t} = G(h_e)\, k \frac{\partial^2 T}{\partial z^2} \tag{1}$$

where ρ, c_p, and k are the density, specific heat, and thermal conductivity of the material (snow or ice), respectively; T is the temperature; t is the time; and z is the vertical coordinate. (The numerical values of the model constants and parameters are listed in Table 1.) $G(h_e)$ is a correction factor that accounts for the fact that the unresolved ice floes of varying thickness contribute differently to the average heat conduction [*Mellor and Kantha*, 1989]. Assuming that the snow and ice thicknesses are uniformly distributed between zero and twice their mean value over the ice-covered part of the grid cell and ignoring the heat capacity of the system, one has (see the appendix for details)

$$G(h_e) = 1 + \frac{1}{2} \ln\left(\frac{2h_e}{e\epsilon}\right) \tag{2}$$

Table 1. Numerical Values of the Model Constants and Parameters

Symbol	Definition	Value
c_{pi}	specific heat of sea ice	2093 J kg^{-1} K^{-1}
c_{ps}	specific heat of snow	2093 J kg^{-1} K^{-1}
c_{pw}	specific heat of seawater	4001.896 J kg^{-1} K^{-1}
C	ice strength parameter	20
C_{wi}	water drag coefficient	5.5×10^{-3}
γ_r	relaxation constant	3.171×10^{-8} s^{-1} (= 1 yr^{-1})
D	horizontal diffusivity	300 m^2 s^{-1}
e_c	eccentricity of the yield curve	2
ϵ	threshold thickness for the computation of $G(h_e)$	0.1 m
ε_{su}	emissivity of snow or ice	0.97
ε_w	emissivity of seawater	0.97
g	acceleration due to gravity	9.80665 m s^{-2}
h_0	thickness of newly formed ice in leads	0.5 m
θ	boundary layer turning angle (ocean)	+25° (NH); −25° (SH)
k_i	thermal conductivity of sea ice	2.0344 W m^{-1} K^{-1}
k_s	thermal conductivity of snow	0.3098 W m^{-1} K^{-1}
k_S	vertical diffusivity of salt in the pycnocline	2×10^{-5} m^2 s^{-1}
k_T	vertical diffusivity of heat in the pycnocline	2×10^{-5} m^2 s^{-1}
L_i	volumetric latent heat of fusion of sea ice	300.330×10^6 J m^{-3}
L_s	volumetric latent heat of fusion of snow	110.121×10^6 J m^{-3}
$\frac{1}{2\epsilon_0}P$	maximum compressive ice viscosity	$(0.55 \times 10^7$ s$)\ P$
P^*	ice strength parameter	5000 N m^{-2}
R	Earth's radius	6.378×10^6 m
ρ_i	density of sea ice	900 kg m^{-3}
ρ_s	density of snow	330 kg m^{-3}
ρ_w	reference density of seawater	1024.458 kg m^{-3}
S_i	salinity of sea ice	4 psu
σ	Stefan-Boltzmann constant	5.67×10^{-8} W m^{-2} K^{-4}
T_{fi}	melting point of sea ice	273.05 K
T_{fs}	melting point of snow	273.15 K
Ω	Earth's angular velocity	7.2722×10^{-5} s^{-1}

NH is northern hemisphere; SH is southern hemisphere.

In this expression, e is the base of the natural logarithms and h_e is an effective thickness for heat conduction defined as

$$h_e = \frac{k_s k_i}{k_s + k_i}\left(\frac{h_s}{k_s} + \frac{h_i}{k_i}\right) \tag{3}$$

where the subscripts s and i stand for snow and ice, respectively, and h is the mean thickness. The threshold thickness ϵ determines the limit of validity of (2). For $h_e < e\epsilon/2$, $G(h_e)$ is taken equal to 1. It should be noted that a more realistic thickness distribution than the one assumed to derive (2) can be obtained from multilevel dynamic calculations [e.g., *Hibler*, 1980; *Flato and Hibler*, 1995] using the ice thickness distribution theory developed by *Thorndike et al.* [1975]. Thus the treatment employed here must be regarded as a first attempt to implicitly include a range of thicknesses in the model thermodynamics.

At the surface of the snow-ice system, a balance of fluxes is supposed to exist, so that

$$B_{su}(T_{su}) = (1 - i_0)(1 - \alpha_{su})F_{sw} + \varepsilon_{su}F_{lw} - \varepsilon_{su}\sigma T_{su}^4 + F_h + F_{le} + F_{cs} = 0 \tag{4}$$

where the subscript su refers to a property of the top surface (snow or ice), F_{sw} is the incoming shortwave radiation, α is the albedo, i_0 is the fraction of the net shortwave radiation that penetrates the snow or bare ice, F_{lw} is the incoming longwave radiation, ε is the emissivity, σ is the Stefan-Boltzmann constant, F_h and F_{le} are the turbulent fluxes of sensible heat and latent heat, respectively, and F_{cs} is the conductive heat flux from below the surface. A flux toward the surface is taken to be positive, while one away from the surface is taken to be negative. We follow *Maykut and Untersteiner* [1971] in setting i_0 equal to 0 in the case of snow-covered ice. When the ice is free of snow, i_0 is parameterized as [*Ebert and Curry*, 1993]

$$i_0 = 0.18\ (1 - c) + 0.35\ c \tag{5}$$

where c is the fractional cloud amount. As it is apparent from (5), the amount of solar radiation transmitted into the ice interior is larger for overcast than for clear conditions. This results from the combined effect of multiple reflections between the surface and the base of clouds and of selective absorption by clouds of the less reflective longwave radiation [*Grenfell and Maykut*, 1977]. If

the heat balance (4) requires the surface temperature T_{su} to be above the melting point (T_{fs} for snow and T_{fi} for ice), T_{su} is held at that point and the excess of energy is balanced by melting snow or ice:

$$\left(\frac{\partial h_s}{\partial t}\right)_{su,abl} = -\frac{B_{su}(T_{su})}{L_s} \qquad h_s > 0 \qquad (6)$$

$$\left(\frac{\partial h_i}{\partial t}\right)_{su,abl} = -\frac{B_{su}(T_{su})}{L_i} \qquad h_s = 0 \qquad (7)$$

where L_s and L_i are the volumetric latent heats of fusion of snow and ice, respectively. Solid precipitation represents the only source of mass at the surface. When the load of snow is large enough to depress the lower boundary of the snow layer under the water level, seawater is assumed to infiltrate the entirety of the submerged snow and to freeze there, forming a snow ice cap. Neglecting the settling of snow due to flooding and the difference of density between snow ice and ordinary ice, the changes of snow and ice thicknesses associated with this snow ice formation are given by

$$-(\Delta h_s)_{si} = (\Delta h_i)_{si} = \frac{\rho_s h_s - (\rho_w - \rho_i) h_i}{\rho_s + \rho_w - \rho_i} \qquad (8)$$

where ρ_w is the reference density of seawater. In this parameterization, the total mass of newly formed snow ice $\rho_i (\Delta h_i)_{si}$ consists of a meteoric ice contribution from the soaked snow $\rho_s (\Delta h_s)_{si}$ and a contribution from the infiltrated seawater $(\rho_i - \rho_s)(\Delta h_i)_{si}$. The latent heat and the brine released in the freezing of the seawater component are discharged into the mixed layer. While natural conditions are not fully represented in such a simplified scheme (see, for example, *Eicken et al.* [1994] and *Jeffries et al.* [1994]), it leads to a geographical distribution of snow ice thickness that is consistent with observations (T. Fichefet and M. A. Morales Maqueda, On the importance of snow ice formation in large-scale sea ice simulations, manuscript in preparation, 1997). Upon an episode of snow ice formation, the internal temperatures of the ice cover are recomputed by a weighted formula.

The mechanism of "brine damping" has been incorporated in the model following the approach of *Semtner* [1976], wherein the solar energy absorbed inside the ice is stored in a heat reservoir that represents internal meltwater. Energy from this reservoir Q_{st} is used to keep the temperature of the upper ice layer from dropping below the freezing point in autumn, thereby simulating the release of latent heat through refreezing of the internal brine pockets. Assuming an exponential absorption of shortwave radiation within the ice [*Grenfell and Maykut*, 1977], Q_{st} evolves according to

$$\frac{\partial Q_{st}}{\partial t} = i_0 (1 - \alpha_{su}) F_{sw} \left[1 - e^{-1.5\,(h_i - 0.1)}\right] - F_{lbp} \qquad (9)$$

where F_{lbp} is the heat flux necessary to prevent the upper ice layer from cooling below T_{fi}. The heat reservoir is restricted to accumulating 50% of the energy required to melt the whole ice sheet. The value chosen for the restriction is somewhat arbitrary but is needed to prevent the model from numerically storing more heat than is needed to melt all the ice. Once this limit is reached, the shortwave radiation absorbed inside the ice contributes to the ice melting.

At the bottom of the ice slab, any imbalance between the conductive heat flux within the ice F_{cb} and the heat flux from the ocean to the ice F_w is compensated by an accretion or ablation of ice:

$$\left(\frac{\partial h_i}{\partial t}\right)_{b,acc-abl} = \frac{F_{cb} - F_w}{L_i} \qquad (10)$$

The oceanic heat flux F_w is computed by imposing a thermodynamic equilibrium between sea ice and the water underneath (see section 2.3 for the formulation of F_w). Therefore both the temperature at the base of the ice and T_m, the mixed layer temperature, are supposed to be equal to the freezing point of seawater T_{fw}, which is determined from *Doronin and Kheisin's* [1977] formula:

$$T_{fw} = 273.15 - (3.0 + 52.75\, S_m + 0.04\, S_m^2 + 0.0004\, S_m^3)\, 10^{-3} \qquad (11)$$

where S_m is the mixed layer salinity.

2.1.2. Lateral growth and decay of the ice. To take into consideration the existence of leads and polynyas within the ice pack, we introduce the concentration variable A, which is defined as the fraction of the grid cell area covered by ice. Variations of A depend on the heat budget of the open water area B_l (the computation of B_l is detailed in section 2.3).

If B_l is negative, ice of thickness h_0 and temperature T_{fw} is accumulated onto the side of the existing ice:

$$\left(\frac{\partial A}{\partial t}\right)_{acc} = \Phi(A) \frac{(1 - A) B_l}{L_i h_0} \qquad (12)$$

where $\Phi(A)$ is a monotone, nonincreasing function such that $\Phi(0) = 1$ and $\Phi(1) = 0$. In many large-scale sea ice models, a minimum lead fraction is prescribed to simulate the fact that cracks or leads are always present inside the pack owing to unresolved dynamical effects. Here we use instead a correction factor $\Phi(A)$ that restrains the closure of leads by partitioning the heat loss B_l between lateral and vertical ice growth. Only a percentage $\Phi(A)$ of the ice formed in the freezing leads contributes to increase the ice concentration. The remaining fraction is rather assumed to lead to an increase in the thickness of the preexisting ice. In spirit, this is similar to the parameterization of *Häkkinen and Mellor* [1992], in which the lead closure rate is slowed down by making h_0 proportional to h_i. We have chosen the following form for $\Phi(A)$:

$$\Phi(A) = (1 - A^2)^{\frac{1}{2}} \qquad (13)$$

A far more physical way of dealing with the opening

of leads during winter would be to take into account the contribution of shearing deformation both to the formation of open water and to ice ridging. *Stern and Rothrock* [1995] have shown how to add these features in two-level sea ice models, which might persuade us to dispose of the ad hoc parameterization presented here and to use their treatment in the near future. Whenever lateral accretion of ice takes place, the thickness of the newly formed ice is averaged with that of the older ice to obtain a single value and the snow is distributed over the new ice-covered area. The internal ice temperatures are modified accordingly.

Numerical experiments conducted by *Steele* [1992], in which the ice cover is approximated by an ensemble of cylindrical ice blocks of variable size, suggest that lateral melting is unimportant for ice floes larger than 30 m in diameter. From this result, we can infer that the summer decrease in ice concentration is, for the most part, caused by the vertical melting of thin ice. Therefore, when B_l is positive, we suppose that the entire heat gain in leads contributes to basal melting through F_w. Assuming that the ice is uniformly distributed in thickness between 0 and $2h_i$ over the ice-covered portion of the grid cell and that the melting rate is independent of the local ice thickness, vertical melting necessarily implies a concomitant reduction in ice concentration given by

$$\left(\frac{\partial A}{\partial t}\right)_{abl} = \frac{A}{2h_i}\,\Gamma\left\{-\left[\left(\frac{\partial h_i}{\partial t}\right)_{acc-abl} + \left(\frac{\partial h_i}{\partial t}\right)_{si}\right]\right\} \tag{14}$$

where Γ is the Heaviside unit function. This parameterization is based on the one proposed by *Häkkinen and Mellor* [1990]. In practice, all the energy available for ice melting is used in the model to promote vertical ablation. Therefore, after determining the decrease in ice concentration by way of (14), the ice thickness must be corrected accordingly so as to conserve ice volume. When the ice concentration decreases, the snow present at the surface of the removed ice is piled up onto the remaining ice.

2.1.3. Ice dynamics. For the momentum balance, the ice is considered as a two-dimensional continuum in dynamical interaction with the atmosphere and ocean. The advection of momentum is neglected. This is a quite reasonable approximation since it has been shown by scale analysis [e.g., *Thorndike*, 1986a] that for time averages above half an hour, inertial forces due to ice acceleration are small compared with other forces acting on the pack. Thus the momentum equation reduces to

$$m\,\frac{\partial \mathbf{u}}{\partial t} = -mf\mathbf{k}\times\mathbf{u} + \boldsymbol{\tau}_{ai} + \boldsymbol{\tau}_{wi} - mg\nabla\xi + \mathbf{F} \tag{15}$$

where m is the mass of the snow-ice system per unit area, $\mathbf{u}$ is the sea ice velocity, f is the Coriolis parameter, $\mathbf{k}$ is the upward unit normal, $\boldsymbol{\tau}_{ai}$ and $\boldsymbol{\tau}_{wi}$ are the forces per unit area due to air and water drags, respectively, g is the acceleration due to gravity, ξ is the sea surface dynamic height, and $\mathbf{F}$ is the force per unit area due to variations in internal ice stress.

The internal ice force can be written in terms of the divergence of the two-dimensional stress tensor, $\mathbf{F} = \nabla\cdot\boldsymbol{\sigma}$. Following *Hibler* [1979], sea ice is assumed to have a viscous-plastic constitutive law:

$$\boldsymbol{\sigma} = 2\eta\dot{\boldsymbol{\epsilon}} + \left[(\zeta-\eta)\,T(\dot{\boldsymbol{\epsilon}}) - \frac{P}{2}\right]\mathbf{I} \tag{16}$$

where η and ζ are shear and bulk viscosities, respectively, $\dot{\boldsymbol{\epsilon}}$ is the strain rate tensor, $T(\dot{\boldsymbol{\epsilon}})$ is the trace of $\dot{\boldsymbol{\epsilon}}$, P is the ice strength, and $\mathbf{I}$ is the two-dimensional unity tensor. The viscosities ζ and η depend on the two invariants of the tensor $\dot{\boldsymbol{\epsilon}}$ (i.e., its trace and its determinant) and on P:

$$\zeta = \frac{P}{2\Delta} \qquad \eta = \frac{\zeta}{e_c^2} \tag{17}$$

where

$$\Delta = \max\left\{\dot{\epsilon}_0, \left[T^2(\dot{\boldsymbol{\epsilon}})\left(1+\frac{1}{e_c^2}\right) - D(\dot{\boldsymbol{\epsilon}})\,\frac{4}{e_c^2}\right]^{\frac{1}{2}}\right\} \tag{18}$$

e_c is the ratio of the principal axes of the elliptical yield curve, $D(\dot{\boldsymbol{\epsilon}})$ is the determinant of the strain rate tensor, and $\dot{\epsilon}_0$ is a parameter termed "creep limit". This rheology allows sea ice to flow plastically for normal strain rates and to deform in a linear viscous manner for very small strain rates. It is commensurate with the physics of ridge building and lead formation and supplies a consistent way of modeling ice drift near and far from shore [*Hibler*, 1979]. In accordance with *Hibler* [1979], the ice strength is parameterized as

$$P = P^* A\, h_i\, e^{-C\,(1-A)} \tag{19}$$

where P^* and C are empirical constants. Note that the contribution of snow to P is ignored.

2.1.4. Continuity equations. The physical fields that are advected are the ice concentration A, the snow volume per unit area Ah_s, the ice volume per unit area Ah_i, the snow enthalpy per unit area AQ_s (with $Q_s = \rho_s c_{ps}\int_0^{h_s} T_s(z)\,dz$), the ice enthalpy per unit area AQ_i (with $Q_i = \rho_i c_{pi}\int_0^{h_i} T_i(z)\,dz$), and the latent heat contained in the brine reservoir per unit area AQ_{st}. Local changes in these variables are computed from the following general conservation law

$$\frac{\partial \Psi}{\partial t} = -\nabla\cdot(\mathbf{u}\Psi) + D\nabla^2\Psi + S_\Psi \tag{20}$$

where Ψ represents any of the variables listed above, S_Ψ is the rate of change of Ψ due to thermodynamics, and D is a horizontal diffusivity. Although, in practice, there may be some actual diffusion in the ice field due to random effects [*Thorndike*, 1986b], the diffusion term used in (20) must be viewed as a numerical artifact to avoid nonlinear instabilities arising from the coupling between ice dynamics and transport. The diffusivity D

takes a constant value inside the pack and is set equal to 0 at the ice edge.

2.2. Upper Ocean Model

The upper ocean model is one-dimensional and consists of an integral mixed layer model coupled to a diffusive model of the pycnocline. The governing equations for the mixed layer temperature and salinity are

$$\rho_w c_{pw} h_m \frac{\partial T_m}{\partial t} = F_{sol}\,[1 - i_w(-h_m)] + F_{nsol} - \rho_w c_{pw} w_e \Delta T - \rho_w c_{pw} k_T \left(\frac{\partial T}{\partial z}\right)_{-h_m} + (F_{caT})_{-h_m} + \rho_w c_{pw} h_m \gamma_r (T_m^* - T_m) \quad (21)$$

$$\rho_w h_m \frac{\partial S_m}{\partial t} = F_{\mathrm{salt}} - \rho_w w_e \Delta S - \rho_w k_S \left(\frac{\partial S}{\partial z}\right)_{-h_m} + (F_{caS})_{-h_m} + \rho_w h_m \gamma_r (S_m^* - S_m) \quad (22)$$

where c_{pw} is the specific heat of seawater, h_m is the mixed layer depth, F_{sol} is the net shortwave radiation at the surface, $i_w(z)$ is the fraction of the net shortwave radiation that penetrates to the depth z in the ocean (parameterized as a function of *Jerlov*'s [1976] water type following *Paulson and Simpson* [1977]), F_{nsol} is the net nonsolar heat flux at the surface (i.e., the sum of all surface heat fluxes except F_{sol}), F_{salt} is the surface salt flux, w_e is the entrainment velocity ($w_e = \Gamma(\partial h_m/\partial t)$), ΔT and ΔS are the temperature and salinity jumps across the mixed layer base, respectively, k_T and k_S are the diffusivities of heat and salt below the mixed layer, respectively, and F_{caT} and F_{caS} are the respective fluxes of heat and salt due to overturning episodes (see section 2.4). Note that T_m and S_m are relaxed toward climatological values via the terms $\rho_w c_{pw} h_m \gamma_r (T_m^* - T_m)$ and $\rho_w h_m \gamma_r (S_m^* - S_m)$, where γ_r is the inverse of a time constant, $T_m^* = h_m^{-1} \int_{-h_m}^{0} T^* dz$, and $S_m^* = h_m^{-1} \int_{-h_m}^{0} S^* dz$, with T^* and S^* the depth-dependent reference temperature and salinity, respectively. These terms have been introduced to compensate for the absence of ocean dynamics in the model, which precludes a prognostic computation of the horizontal transport and redistribution of heat and salt in the ocean. The restoring on salinity also helps to rectify the undesirable effects due to the lack of runoff forcing in our simulations and to the rather poor quality of available precipitation data. In the present application, the reference temperatures and salinities are annual mean observed data (see section 2.5) and, accordingly, $\gamma_r = 1\ \mathrm{yr}^{-1}$. The third and fourth terms on the right-hand side of (21) represent the entrainment and diffusion heat fluxes at the base of the mixed layer. These terms together with the relaxation term in (21) will be hereafter referred to as F_{ent}, F_{dif}, and F_{rel}, respectively.

In the pycnocline, the temperature and salinity evolve according to

$$\frac{\partial T}{\partial t} = \frac{F_{sol}}{\rho_w c_{pw}} \frac{\partial i_w}{\partial z} + k_T \frac{\partial^2 T}{\partial z^2} + \frac{1}{\rho_w c_{pw}} \frac{\partial F_{caT}}{\partial z} + \gamma_r (T^* - T) \quad (23)$$

$$\frac{\partial S}{\partial t} = k_S \frac{\partial^2 S}{\partial z^2} + \frac{1}{\rho_w} \frac{\partial F_{caS}}{\partial z} + \gamma_r (S^* - S) \quad (24)$$

The first term on the right-hand side of (23) represents the differential absorption of the shortwave radiation that after entering the ocean through leads and ice, traverses the whole depth of the mixed layer. This trapping of solar energy mainly occurs during summer months, when the mixed layer is shallow. The absorbed energy is progressively released in the mixed layer during fall as the upper ocean destratifies. *Perovich and Maykut* [1990] have discussed the potential importance of this phenomenon in limiting ice growth in regions of relatively static ice and limited ocean motion.

To close the system, an equation for h_m is required. It is classically obtained from considerations on the turbulent kinetic energy budget of the mixed layer. Here we use *Gaspar*'s [1988] formulation that was specifically designed for simulations at the seasonal timescale. This parameterization is documented by *Fichefet and Gaspar* [1988].

2.3. Coupling of the Sea Ice and Upper Ocean Models

The sea ice model determines the surface boundary conditions of the upper ocean model, i.e., the heat, salt, and momentum fluxes entering the mixed layer from the top. The ocean model, in turn, supplies the exchange of sensible heat at the ice-water interface.

The net shortwave radiation at the ocean surface can be expressed as

$$F_{sol} = A\,F_{str} + (1 - A)\,(1 - \alpha_w)\,F_{sw} \quad (25)$$

where F_{str} is the shortwave radiation reaching the base of the ice cover ($F_{str} = i_0 (1 - \alpha_{su}) F_{sw} \exp[-1.5\,(h_i - 0.1)]$) and α_w is the albedo of the open ocean. In the grid cells totally free of ice, the nonsolar surface heat flux is given by

$$F_{nsol} = \varepsilon_w F_{lw} - \varepsilon_w \sigma T_m^4 + F_h + F_{le} - F_{lpr} \quad (26)$$

where ε_w is the emissivity of seawater and F_{lpr} is the latent heat flux associated with the melting of snow falling onto the ocean. In the presence of sea ice, we set

$$F_{nsol} = -F_{sol}\,[1 - i_w(-h_m)] \quad (27)$$

Snow and ice melting, salt rejection during ice accretion and snow ice formation, evaporation at the lead surface, and precipitation all contribute to the surface salt flux:

$$F_{\text{salt}} = S_m \left(\frac{\partial m_s}{\partial t}\right)_{abl} + (S_m - S_i)\left(\frac{\partial m_i}{\partial t}\right)_{acc-abl} + (S_m - S_i)\left(\frac{\partial m_s}{\partial t} + \frac{\partial m_i}{\partial t}\right)_{si} + S_i \left(\frac{\partial m_s}{\partial t}\right)_{si} + S_m (AE - P_w) \quad (28)$$

where m_s and m_i are the masses of snow and ice per unit area, respectively, S_i is the sea ice salinity, E is the evaporation rate over the lead area, and P_w is the rate of freshwater supplied by precipitation (P_w includes the contributions from the rain and from the snow falling onto open water and melting sea ice). The third and fourth terms on the right-hand side of (28) are salt fluxes resulting from snow ice formation. The first of these fluxes mimics the salt rejection that arises when the seawater infiltrating the submerged snow freezes, whereas the second one is an artificial flux which provides the meteoric ice with the adequate salinity.

Both the input of turbulent kinetic energy into the mixed layer and the shear production are parameterized in terms of the cube of the friction velocity u_*, which accordingly is computed over each model grid as

$$u_* = \left[A\, u_{*i}^3 + (1 - A)\, u_{*a}^3\right]^{\frac{1}{3}} \quad (29)$$

where u_{*i} and u_{*a} are the friction velocities at the ice-water and air-water interfaces, respectively. Assuming the continuity of the stresses across these interfaces, one obtains

$$u_{*i} = \left(\frac{|\tau_{wi}|}{\rho_w}\right)^{\frac{1}{2}} \qquad u_{*a} = \left(\frac{|\tau_{aw}|}{\rho_w}\right)^{\frac{1}{2}} \quad (30)$$

where τ_{aw} is the wind stress over ice-free water. The stress τ_{wi} is obtained from a simple quadratic formulation [*Hibler*, 1979]:

$$\tau_{wi} = \rho_w C_{wi} |\mathbf{u}_w - \mathbf{u}| [(\mathbf{u}_w - \mathbf{u}) \cos\theta + \mathbf{k} \times (\mathbf{u}_w - \mathbf{u}) \sin\theta] \quad (31)$$

where C_{wi} is a drag coefficient, $\mathbf{u}_w$ is a climatological geostrophic ocean current, and θ is a boundary layer turning angle.

In ice-covered regions, the sensible heat flux from the ocean to the ice F_w and the heat balance of the leads B_l have to be determined. As mentioned before, we suppose that sea ice is in thermodynamic equilibrium with the underlying mixed layer ($T_m = T_{fw}$). To maintain this equilibrium, F_w must compensate exactly for the net heat gain of the mixed layer:

$$F_w = [1 - i_w(-h_m)]\, F_{str} + F_{ent} + F_{dif} + (F_{caT})_{-h_m} + F_{rel} + F_{fus} + \Gamma\left[\frac{(1 - A)\, B_l}{A}\right] \quad (32)$$

where F_{fus} is the heat flux released or absorbed by the mixed layer to follow the variations of T_{fw} due to changes in salinity ($F_{fus} = -\rho_w c_{pw} h_m (\partial T_{fw}/\partial t)$). The first six fluxes on the right-hand side of (32) result from processes occurring directly under the ice (their sum will be hereafter referred to as F_{wv}), while the seventh flux (hereafter F_{wl}) originates from the lead area. The heat budget of the leads is expressed as

$$B_l = [1 - i_w(-h_m)](1 - \alpha_w) F_{sw} + \varepsilon_w F_{lw} - \varepsilon_w \sigma T_m^4 + F_h + F_{le} + F_{lsi} - F_{lpr} + F_{ent} + F_{dif} + (F_{caT})_{-h_m} + F_{rel} + F_{fus} \quad (33)$$

where F_{lsi} is the latent heat release accompanying snow ice formation ($F_{lsi} = [(\rho_i - \rho_s)/\rho_i]\, L_i\, (\partial h_i/\partial t)_{si}$).

2.4. Numerical Framework

The model equations are solved numerically as an initial value–boundary value problem by using finite difference techniques. A staggered spatial grid of type B [*Arakawa*, 1966] is employed.

The heat diffusion equation for snow and ice (equation (1)) is solved by means of a fully implicit numerical scheme, which avoids the development of numerical instabilities when the snow or ice thickness becomes small. In order to ensure that the heat balance at the top surface of the snow-ice system is strictly satisfied, (4) is solved iteratively for T_{su} by a Newton-Raphson procedure. The ice momentum balance (equation (15)) is treated basically as by *Hibler* [1979], the two main differences being that we do not linearize the oceanic drag term and that we systematically apply a simultaneous underrelaxation technique. A no-slip condition is imposed at land boundaries. To perform the simulations discussed below, the model has been installed on a standard latitude-longitude grid for which (15) has a singular point at the north pole. To cope with this singularity, the ice velocity at 90°N is taken as the mass-weighted vectorial average of the velocities located immediately to the south. The contribution of advection to (20) is determined by making use of the forward time marching scheme of *Prather* [1986]. This method is based on the conservation of the second-order moments of the spatial distribution of the advected quantities within each grid cell. It preserves the positiveness of the transported variables and presents very small diffusion. The interest of employing this elaborate scheme is that for a coarse resolution grid such as the one used here (see section 2.5), it allows to determine the location of the ice edge with a higher accuracy than more conventional upstream schemes do. The diffusion component of (20) is also solved explicitly. Worthy of note is that the equations for both ice motion and ice transport are written in curvilinear, orthogonal coordinates, which facilitates the model setup on a large variety of spatial grids.

The numerical solution of the mixed layer–pycnocline equations (21)–(24) follows *Fichefet and Gaspar* [1988]. Convective adjustment occurs whenever the water column becomes statically unstable. The scheme employed here [*Marotzke*, 1991] guarantees complete vertical stability at the end of each time step. No flux of heat or salt is permitted at the base of the oceanic domain.

2.5. Grid Configuration and Forcing

The model domain is global. A spherical grid identical to that of spectral T42 atmospheric general circulation models is used. The resolution is Gaussian in latitude and uniform in longitude. At the equator, the grid cells are squares of $2.8125° \times 2.8125°$, some 315 km in length, while at the poles, they are triangles with a base of about 20 km. The upper ocean model includes a maximum of 12 vertical levels. The bases of the corresponding layers lie at the following depths: 5, 10, 20, 30, 40, 50, 75, 100, 150, 200, 250, and 300 m. The time step is 1 day for all the model components.

The surface thermal forcing (i.e., the net shortwave radiation, the incoming longwave radiation, the sensible heat flux, and the latent heat flux) and the wind stress over open water areas are determined from empirical parameterizations described by *Fichefet and Gaspar* [1988]. The stress at the air-ice interface is calculated by using the formula recommended by *Overland and Colony* [1994]. Input fields consists of monthly climatological surface air temperatures and dew points [*Crutcher and Meserve*, 1970; *Taljaard et al.*, 1969], surface geostrophic winds [*Crutcher and Meserve*, 1970; *Taljaard et al.*, 1969], precipitation rates [*Jaeger*, 1976], and cloud fractions [*Berliand and Strokina*, 1980]. The fraction of precipitation falling as snow f_s is determined as by *Ledley* [1985]. In essence, f_s is a piecewise linear function of the surface air temperature T_a, which increases monotonously from $f_s\,(T_a \geq 8°\,\mathrm{C}) = 0$ to $f_s\,(T_a \leq -20°\,\mathrm{C}) = 1$. The surface geostrophic currents used to compute the water stress on ice and the tilt term $-mg\nabla\xi\ (= mf\mathbf{k} \times \mathbf{u}_w)$ in the momentum balance (15) are obtained from the annual mean temperature and salinity fields of *Levitus* [1982] by applying the variational inverse modeling technique of *Peggion* [1987]. The restoring temperatures and salinities appearing in (21)–(24) are also taken from the annual mean climatology of *Levitus* [1982]. Regarding the ocean turbidity, we use the geographical distribution of *Jerlov*'s [1976] water types proposed by *Simonot and Le Treut* [1986].

Among the forcing fields of the model, the surface air temperatures and geostrophic winds are certainly the key ones; these are depicted, on an annual average, in Figure 1. It should be mentioned here that the charts displayed, as any of the other plots of two-dimensional fields shown in this paper, have been obtained by interpolating the original fields onto a $1° \times 1°$ spherical grid whose axis is tilted by 90° with respect to the Earth's axis. In this grid, the "north pole" is located at the point with geographical coordinates (0°E, 0°N) and the line of 0° longitude passes through the geographical south pole. Fields on this interpolating grid are displayed using a cylindrical, equidistant projection [*Snyder and Voxland*, 1989]. The reason we have performed such data interpolation is that when vectors are plotted on the actual model grid, they appear arranged in concentric circles (the parallels), an organization that becomes increasingly conspicuous and distracting upon approaching the poles, up to the point of masking the physical patterns in the field. For consistency, the same transformation has been applied to the plotted scalar fields.

3. Control Simulation

The model described above was integrated for 10 years, with the same atmospheric and oceanic forcing fields being repeated each year. The integration began on March 1. The initial position of the ice edge was determined by imposing the presence of sea ice in those grid cells where the March sea surface temperature of *Levitus* [1982] is lower than 0°C in the northern hemisphere (NH) and lower than −1°C in the southern hemisphere (SH). The initial values of ice concentration, snow thickness, and ice thickness were 90%, 0.3 m, and 3 m, respectively, in the NH and 60%, 0.3 m, and 1 m, respectively, in the SH. The snow and ice temperatures were initialized to T_{fw}, and the brine reservoir was assumed to be empty everywhere. Motion of both ice packs was started from a state of rest. *Levitus*' [1982] March temperatures and winter salinities were used to initialize the ocean model. A σ_t criterion of 0.125 kg m^{-3} [*Levitus*, 1982] was applied to obtain the initial mixed layer depths. Wherever ice was present, the mixed layer temperature was set equal to T_{fw}. The constraints imposed on the model by the seasonal atmospheric forcing and by the relaxation to annual mean oceanic data were strong enough to preclude any significant interannual variability in the model fields. In particular, the total ice volume reached a cyclostationary equilibrium with an accuracy of 1% in both hemispheres, and this was well before the 10th year of integration, from which the results discussed below are issued.

Apposite variables to characterize the sea ice areal coverage at the hemispheric scale are the effective ice area, the ice extent, and the area of open water enclosed by the ice-ocean boundary. In the model, the effective ice area is determined by summing the areas of the icy grid cells weighted by their ice concentration. The ice area at a given cutoff concentration A_c is obtained by adding up the areas of the grid cells in which the ice concentration is greater than or equal to A_c. As is customary, the ice area at the 15% concentration will be referred to, in short, as the ice extent. The amount of open water within the pack is given by the difference between the ice extent and the effective ice area.

Figures 2a and 2b display the observed seasonal cycles of ice extent, effective ice area, ice area at the 85% concentration, and open water area in the NH and SH, respectively. These climatological time series have been constructed from measurements made by the scanning multichannel microwave radiometer (SMMR) which operated on board the NASA Nimbus 7 satellite from October 1978 to August 1987 [*Gloersen et al.*, 1992]. The corresponding seasonal cycles produced by the model are shown in Figures 2c and 2d. It can be seen that the model does fairly well in simulating the timing of the maximum and minimum areal coverages of ice. In the NH, both the observed and modeled ice extents and effective ice areas culminate during the first 10 days

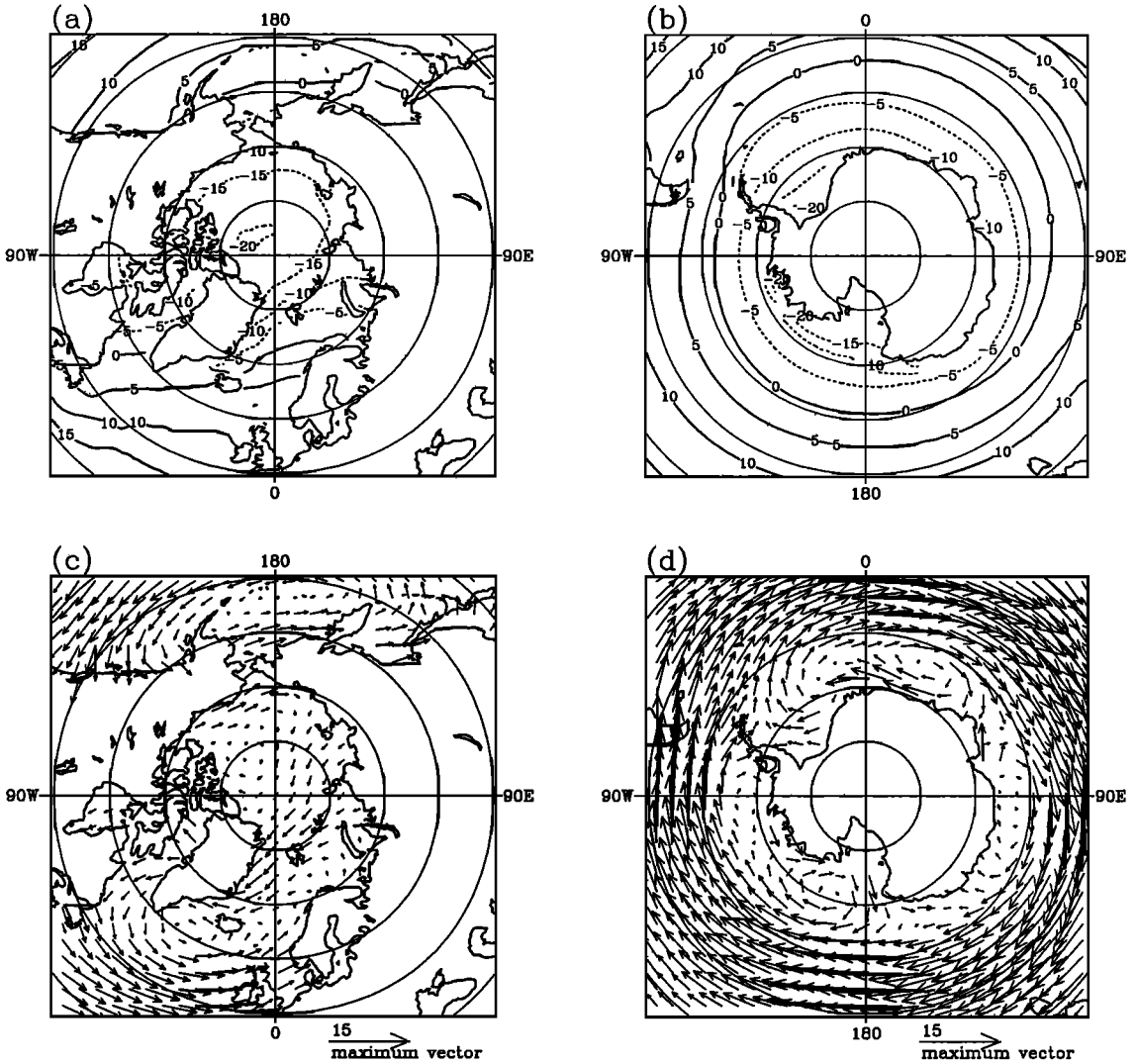

Figure 1. Climatological annual mean surface air temperatures in the (a) northern hemisphere (NH) and (b) southern hemisphere (SH). The contour interval is 5°C. Climatological annual mean surface geostrophic winds in the (c) NH and (d) SH. The scale vector is 15 m s^{-1}.

of March and reach their minimum at the end of the first 10 days or the beginning of the second 10 days of September. In the SH, the observed as well as the computed areal maxima take place by the end of the second 10 days of September, while the minimum occurs during the last 10 days of February in the observations and during the first 10 days of March in the simulation. Because of the coarse resolution of the model grid (the average grid cell area is ~28,750 km^2 in the polar regions), discrepancies of several hundred thousands of square kilometers are to be expected when comparing the predicted ice areal coverages with SMMR estimates, which are derived from a relatively high resolution mapping (the average pixel area is ~2525 km^2). The comparison indicates that the effective ice area simulated in the NH is overestimated by about 1×10^6 km^2 at the winter maximum and is underestimated by about 2×10^6 km^2 at the summer minimum. In the SH, the model overestimates the effective ice area by about 2.5×10^6 km^2 throughout the year. A feature common to both hemispheres is that the model generates a too compact ice cover, as an inspection of the time series of the ice area at the 85% concentration and of the open water area reveals. In the NH, the modeled ice area at the 85% concentration is overestimated by 27% and the computed area of open water is underestimated by 50%, on an annual average. The corresponding errors for the SH are 290% and 30%, respectively. Averaged over the entire seasonal cycle, the mean ice concentration within the pack in the model NH (SH) amounts to 80% (73%), to be compared with the 74% (66%) value derived from the SMMR observations. Reasonably enough, we could put here into question the ability of the model to accurately represent the intricate thermodynamics and dynamics of real leads. However, part of the discrepancy could have its origins elsewhere than in the model itself. First, there is some evidence that the NASA team's algorithm which was used to retrieve the ice concentrations from the satellite measurements underestimates the compactness of the ice cover at high concentrations

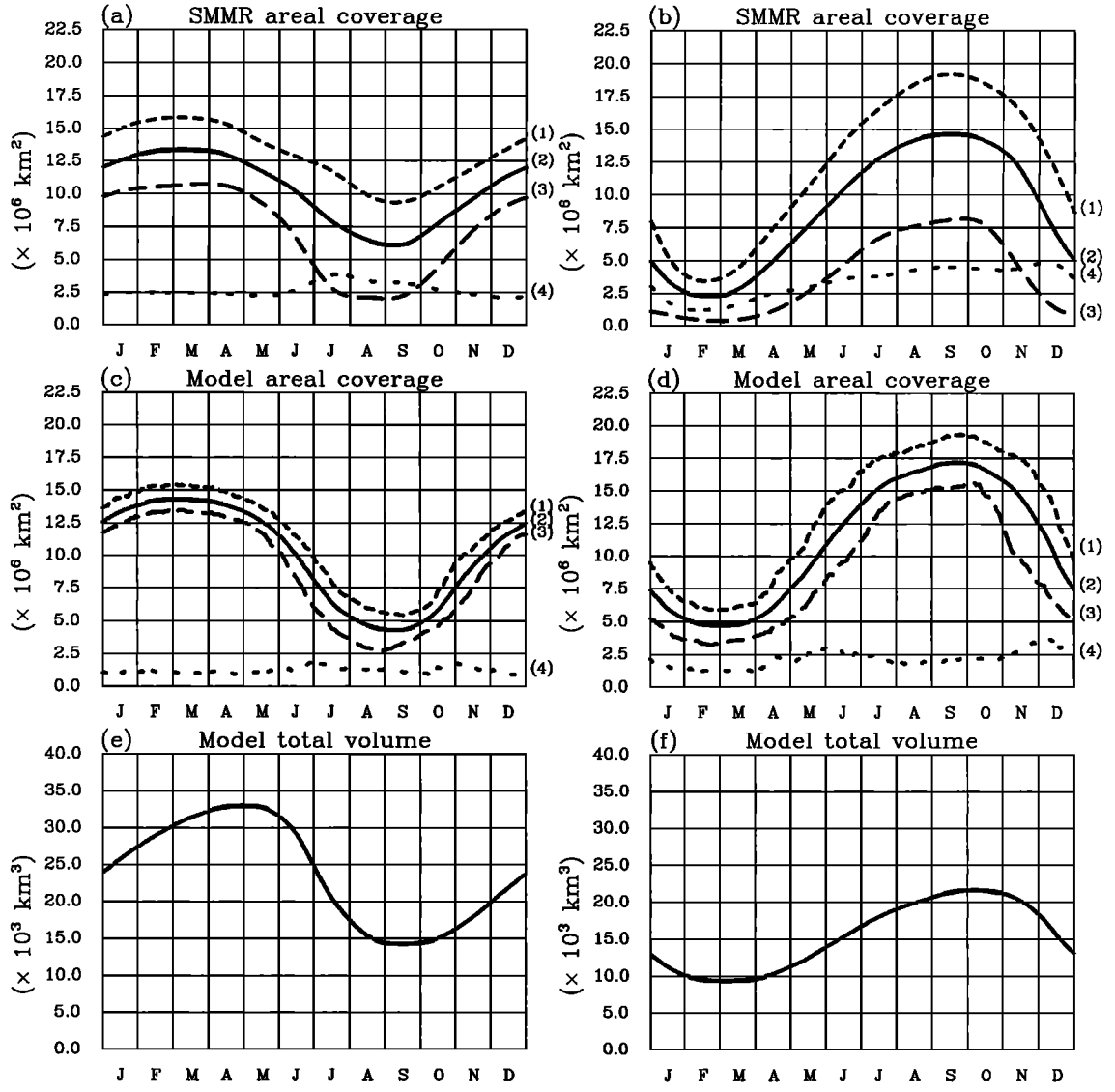

Figure 2. (a) Average seasonal cycle of the ice areal coverage in the NH as determined from the scanning multichannel microwave radiometer (SMMR) data [*Gloersen et al.*, 1992]. Curve labeled 1 shows ice extent; curve labeled 2, effective ice area; curve labeled 3, ice area at the 85% concentration; and curve labeled 4, open water area. (b) Same as Figure 2a, except for the SH. (c) Seasonal cycle of the ice areal coverage in the NH as simulated by the model (control case). Curve labeled 1 shows ice extent; curve labeled 2, effective ice area; curve labeled 3, ice area at the 85% concentration; and curve labeled 4, open water area. (d) Same as Figure 2c, except for the SH. (e) Seasonal cycle of the total ice volume in the NH as simulated by the model (control case). (f) Same as Figure 2e, except for the SH.

(see, for example, the discussions of *Steffen et al.* [1992] and *Cavalieri* [1992]). Second, a modeling study carried out in the SH by *Stössel et al.* [1990] suggests that the daily fluctuations in the wind forcing play an important role in controlling the opening of leads, particularly during winter. Since this variability is not taken into consideration in the present work, the areas of open water simulated by the model are expected to be too small in size.

The seasonal variations of the modeled NH and SH total ice volumes are illustrated in Figures 2e and 2f, respectively. In the NH, the computed ice volume reaches its maximum during the first 10 days of May, i.e., 2 months after the occurrence of the maximum in effective ice area. This phase lag reflects the fact that when the thin ice of the marginal ice zone begins to melt in early spring, occasioning the northward retreat of the ice edge, the thick ice in the central Arctic is still growing. Once the ice melting becomes generalized, the ice volume and the effective ice area evolve in unison, reaching both their minimum in early September. It is noteworthy that the seasonal extrema of the total ice volume and of the average ice thickness obtained by dividing the total ice volume by the effective ice area are

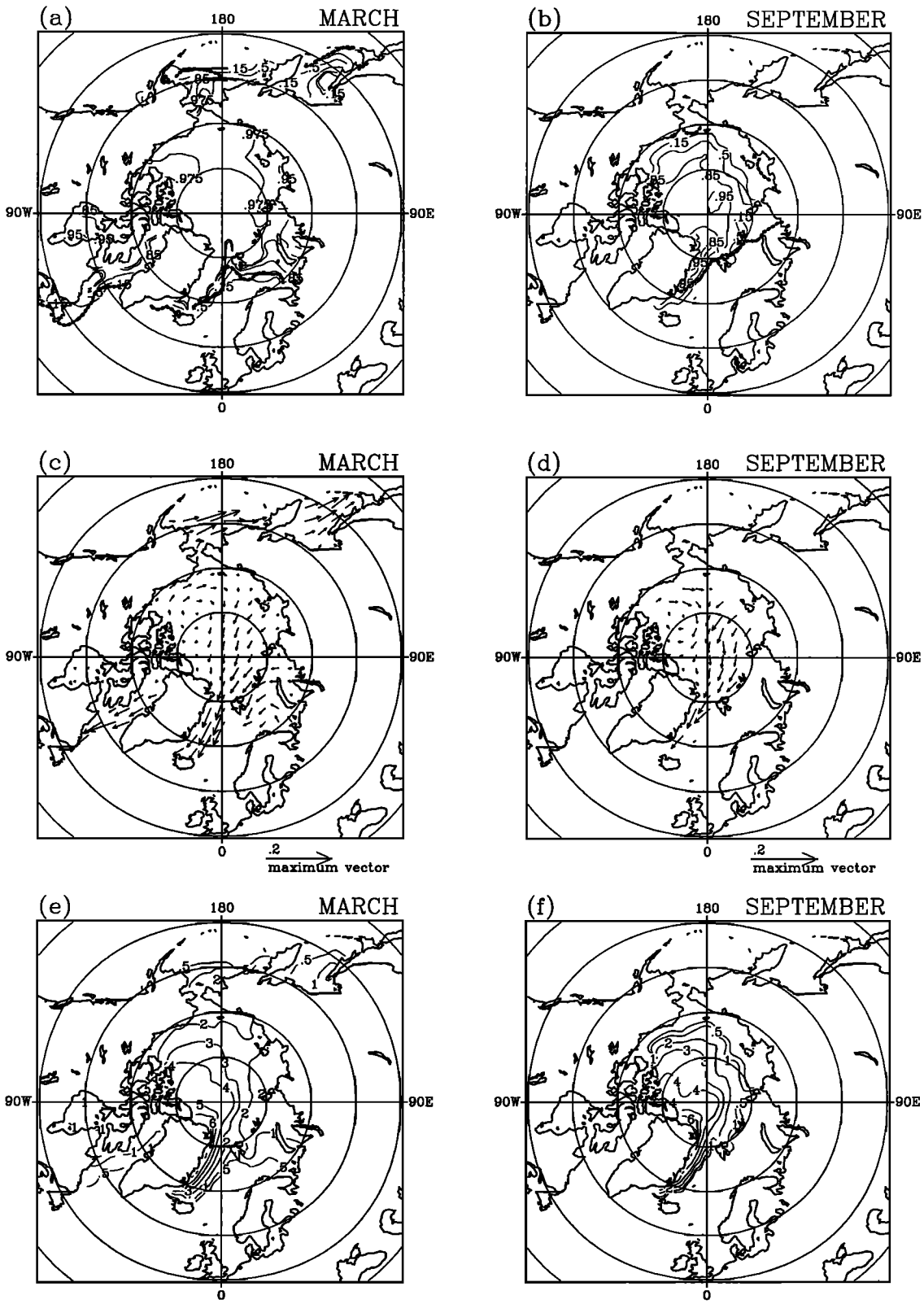

Figure 3. Monthly average fields of (a) March and (b) September ice concentration, (c) March and (d) September ice velocity, and (e) March and (f) September ice thickness for the NH from the control simulation. Selected contours for ice concentration are 0.15, 0.50, 0.85, 0.95, and 0.975. Scale vector for ice velocity is 0.2 m s^{-1}. Selected contours for ice thickness are 0.5, 1, 2, 3, 4, 5, 6, 7, and 8 m. Also shown in Figures 3a and 3b is the 0.15 ice concentration contour as derived from the SMMR data [*Gloersen et al.*, 1992] (thick, stippled line).

out of phase. The average ice thickness peaks at the beginning of August (the maximum value amounts to ~3.3 m), when most of the thin, seasonal ice has disappeared. During autumn, as a result of the growing contribution of the newly formed ice, the average ice thickness steadily diminishes until attaining its minimum (~1.9 m) by mid-December. Since the Antarctic ice pack is thinner and more seasonal than the Arctic one, the simulated maximum ice volume in the SH is delayed by only 2 weeks with respect to the maximum effective ice area, whereas both minima take place at approximately the same date. Regarding the average ice thickness, we encounter here the same kind of behavior as in the NH. The maximum average ice thickness (~2.0 m) occurs at the end of February, while the minimum (~1.2 m) takes place in mid-July.

Figures 3a and 3b depict the March and September geographical distributions of ice concentration, respectively, in the model NH. In March, the modeled location of the ice edge (defined as the 15% concentration contour) agrees relatively well with the observed one (thick, stippled line). One notes, however, that the ice cover protrudes slightly too far eastward in the Greenland Sea and southward in the Norwegian, Barents, and Bering Seas. In addition, the ice edge is somewhat north of the observed edge in the Labrador and Okhotsk Seas. The ice margin simulation is much less satisfactory in September. Ice of concentration less than 50% persists in the southern portion of the Greenland Sea, whereas the observations clearly show that this area is totally free of ice during that part of the year. Furthermore, the ice margin is positioned too far to the north all along the coastal eastern and far western Arctic, leaving a belt of open water running eastward from the Kara Sea through the Laptev, East Siberian, and Chukchi Seas to the Beaufort Sea. We are inclined to attribute this excessive summer retreat of the ice pack to two facts. First, because of the sparsity and rarity of winter field data, the *Levitus'* [1982] data appear to be biased toward warm summer conditions in both hemispheres; thus the relaxation employed in the model has a tendency to melt too much ice. Second, owing to its coarse horizontal resolution and to the absence of a dynamically interactive ocean component, the model is unable to produce realistic enough ice velocities near land boundaries. As demonstrated by *Overland and Pease* [1988], the interplay of ice motion and wind-driven slope currents strongly determines the ice drift and ice thickness patterns in coastal seas, where the offshore component of the momentum balance is basically an equilibrium between the Coriolis force and the force due to the tilt of the sea surface. A correct simulation of the ice drift in the shallow shelf regions of the Arctic Ocean requires therefore a realistic representation of the dynamic topography of the sea surface in these zones. The annual mean geostrophic currents used to drive ice motion in our model are manifestly inappropriate to this purpose. Results from the modeling study of *Häkkinen and Mellor* [1992] seem to support this twofold explanation of the model behavior. These authors employed the same climatological surface air temperatures and geostrophic winds to force a thermodynamic-dynamic sea ice model coupled to a primitive equation model of the Arctic Ocean. Since they were able to explicitly compute the horizontal oceanic heat transport, no restoring to observed temperatures and salinities was applied. The offshore-alongshore resolution along the Eurasian coast was 28 x 150 km, thereby allowing for a relatively reliable simulation of the continental shelf currents. Contrary to our results and in better agreement with the observations, their summer ice cover extents well into the East Siberian and northern Kara Seas.

The simulated ice circulation in the NH (Figures 3c and 3d) exhibits many of the recurrent or permanent features of the observed ice motion (see, for example, *Colony and Thorndike* [1984]). In particular, the clockwise Beaufort Gyre, the Transpolar Drift Stream, and the East Greenland Drift Stream are all well reproduced. The largest monthly mean ice velocities reach ~0.1 m s^{-1} and occur during winter near the ice margin in the Bering and Greenland Seas and in Davis Strait.

On average, the modeled ice drift tends to thin the ice off the Alaskan and Siberian coasts while increasing the ice thickness by convergence and concomitant ridging off the Canadian Archipelago and the north coast of Greenland. In these regions of convergence, ice accumulations of up to ~8 m in thickness are visible throughout the year (Figures 3e and 3f). The shape and magnitude of the simulated ice thickness contours are in general agreement with those derived from submarine sonar measurements (see, for example, *Bourke and Garrett* [1987]). The most flagrant departure from current estimates are observed along the eastern coast of Greenland, where the model generates ice thicknesses of up to ~5.5 m in March and ~4.5 m in September. This abnormal buildup is partly caused by the relatively strong ice outflow simulated through Fram Strait. The simulation yields an annual ice export from the Arctic Ocean to the Greenland Sea via Fram Strait that amounts to ~1.2 x 10^6 km^2 in area and to ~4.2 x 10^3 km^3 in volume (about 0.12 Sv). Although reasonable, these numbers hover around the upper bounds of the observational, albeit rather uncertain, estimates [*Aagaard and Greisman*, 1975; *Englebretson and Walsh*, 1989]. Nevertheless, even with a more moderate ice outflow through Fram Strait, the model is still likely to generate a sizeable ice cover over the Greenland Sea owing to the fact that it has a propensity to exaggerate the stratification of the water column in this region and thus to underestimate the oceanic heat flux responsible for the basal melting of the ice. This behavior is due, on the one hand, to the weakness of the monthly mean wind forcing and, on the other hand, to the simplistic treatment that the model reserves to the lateral heat transport in the ocean, namely, the relaxation of the oceanic temperatures to observed annual mean values. These two factors lead to an underestimation of the mixed layer depth in some key areas of the northern North Atlantic. For instance, the computed mixed layer

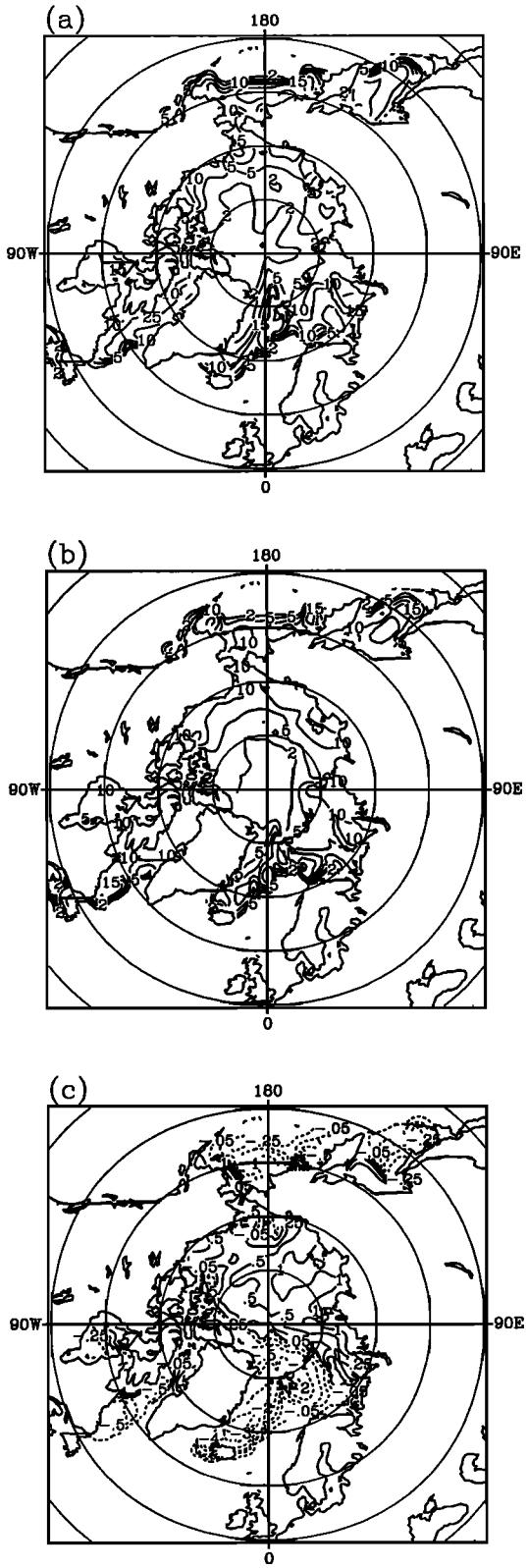

Figure 4. Geographical distribution in the NH of (a) the annually averaged oceanic heat flux component F_{wv}, (b) the annually averaged oceanic heat flux component F_{wl}, and (c) the net annual ice growth/melt (control case). Selected contours for F_{wv} and F_{wl} are 2, 5, 10, 15, 25, 50, 75, and 100 W m^{-2}. Selected contours for net ice growth/melt are ± 0.05, ± 0.25, ± 0.50, ± 1, ± 2, ± 3, ± 4, and ± 5 m yr^{-1}.

depths do not exceed 100 m during winter in the major part of the Norwegian and eastern Greenland Seas. Under the Greenland Sea ice cover, the winter mixed layer is about 35 m deep. During summer months, the mixed layer depths are around 10 m everywhere in the northern North Atlantic. As a result of this stratification, the annual mean oceanic heat losses to the ice, excluding the contribution from leads, are not larger than 60 to 70 W m^{-2} at the ice margin in the Greenland Sea (Figure 4a). Beneath the perennial ice covering the western Greenland Sea, the annual mean value of F_{wv} amounts to $\sim$9 W m^{-2}, on average, which, in addition to another $\sim$9 W m^{-2} originating from the spring and summer leads (Figure 4b), corresponds to a basal melting rate of approximately 0.9 m of ice per year. Under the permanent ice cover in the central Arctic, the upper ocean stratification is much better represented. The average mixed layer depth oscillates there between $\sim$50 m in winter and $\sim$10 m in summer, with accompanying values of F_{wv} ranging from 2–5 W m^{-2} in winter to 0–2 W m^{-2} in summer, in accordance with the few and sparse observations available [*McPhee and Untersteiner*, 1982; *Wettlaufer*, 1991]. On an annual average, F_{wv} and F_{wl} contribute almost equally to the basin-averaged oceanic heat flux ($\sim$11 and $\sim$9 W m^{-2}, respectively), but these contributions barely overlap throughout the year. In fact, F_{wl} takes significant values only from mid-May to mid-September, when F_{wv} is rather weak.

Figure 4c shows the geographical distribution of the modeled net annual ice growth/melt (i.e., the net annual variation of ice thickness due to thermodynamic processes) in the NH. Net ice production takes place almost everywhere in the Arctic, with maximum rates of $\sim$1 m yr^{-1} in the Eurasian side of the basin and in the Beaufort Sea and minimum rates of $\sim$0.25 m yr^{-1} off the Canadian Archipelago. The most active ice growth occurs, however, along the Alaskan coast in the Bering Sea, where a strong ice outflow driven by northerly winds generates up to $\sim$2 m of ice per year. Note that the Chukchi Sea and the areas located just north of Greenland and Spitsbergen are regions of net ice destruction. The zone of the largest net ice melt is the Greenland Sea, where a marked meridional pattern of ablation is apparent: 1.5–2 m yr^{-1} in the Fram Strait, 2–2.5 m yr^{-1} between 80°N and 70°N, and up to 2.5–4 m yr^{-1} in the Denmark Strait. As follows from the previous discussion on the small magnitude of the oceanic heat flux in this region, most of this ice melting takes place at the atmosphere-ice interface.

The March and September ice concentrations simulated by the model in the SH are displayed in Figures 5a and 5b, respectively. As in the NH, the predicted position of the ice edge at the time of the maximum ice extent compares favorably with the observed one (thick, stippled line). The zones of largest discordance are the eastern Atlantic and central Indian sectors of the Southern Ocean, where the observed ice margin advances northward up to 500 km more than the modeled one. It can be argued that the bias of *Levitus'* [1982] data toward fresh summer values could be responsible in

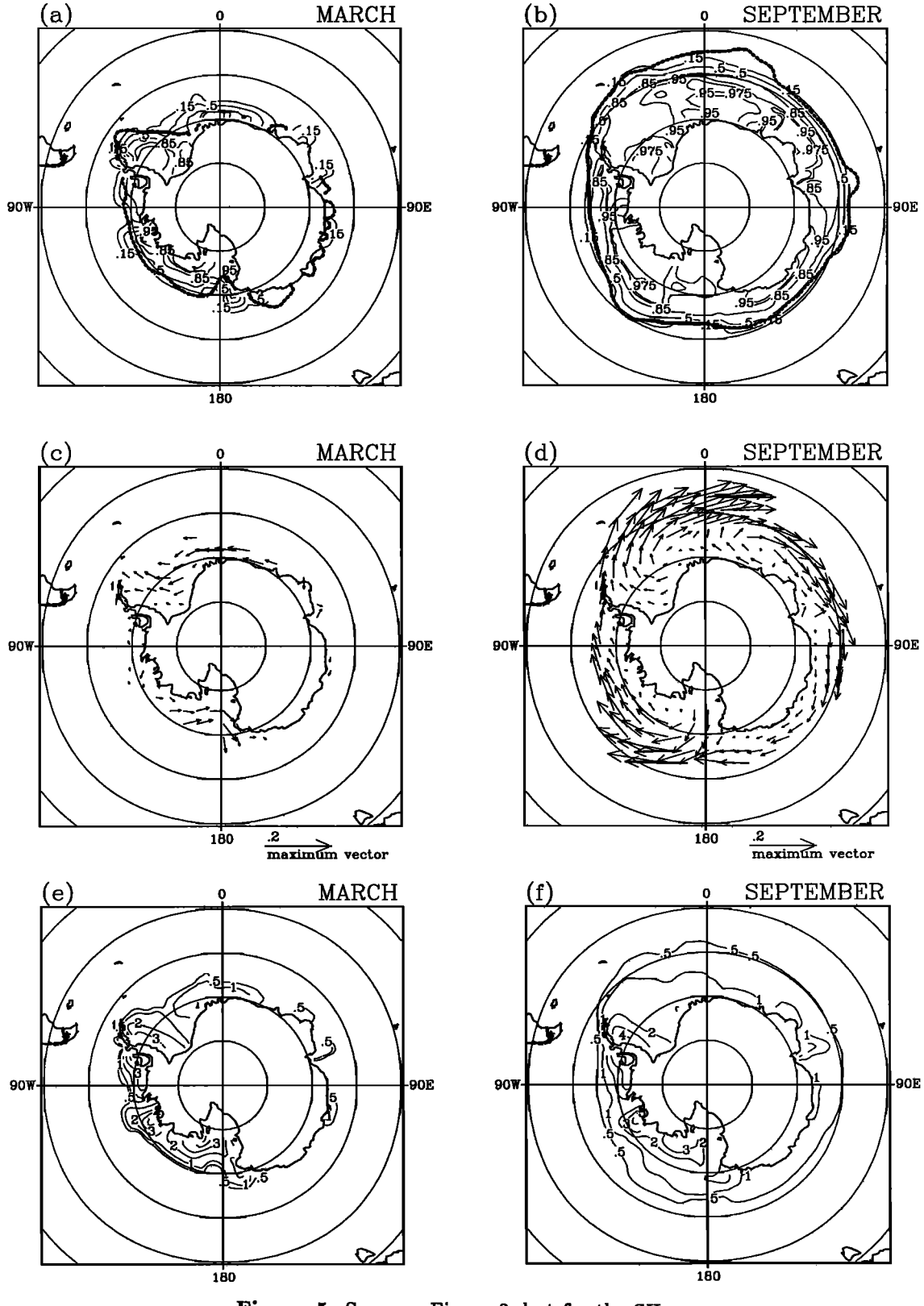

Figure 5. Same as Figure 3, but for the SH.

part for these regional overestimates in the winter sea ice cover. Another factor that must be considered is that in the Southern Ocean, the mixed layer depth can exceed 300 m during the cold months. The bulk of the oceanic sensible heat flux is, in this case, made available from below this depth. The upper ocean model used here is obviously inappropriate to deal with this situation. In sharp contrast with its Arctic counterpart, the simulated Antarctic ice cover is characterized by a relatively uneven distribution of ice concentration

during winter, with alternating areas of tightly packed (>95%) and loosely packed (<95%) ice scattered along the coastal margins and in the pack interior. Very localized minima of ice concentration are apparent in the region of Maud Rise, over the Cosmonaut Sea, and in Prydz Bay, roughly where recurrent polynyas are observed [*Zwally et al.*, 1985; *Comiso and Gordon*, 1987]. The agreement between the simulation and observations falls off sensibly for the summer season. In March, too much ice remains in the eastern Atlantic sector of the Southern Ocean, in the Bellingshausen and Amundsen Seas, and in the western Ross Sea. In the latter region, a large polynya system is observed to develop between December and March as a combined effect of strong katabatic winds blowing from the continent and of warm subsurface water entering the shelf region from the open sea [*Jacobs and Comiso*, 1989]. Our model, in which none of these phenomena is taken into account, produces instead a perennial ice cover in this part of the Ross Sea. On the contrary, most of the the western Pacific sector of the Southern Ocean becomes free of ice during summertime in the model simulation, whereas the observations show a patchy distribution of residual coastal ice there.

Figures 5c and 5d present the predicted ice velocity fields in the SH for March and September, respectively. The model simulates a pronounced Weddell Gyre, a strong offshore ice drift in the Ross Sea, and several smaller gyres along the coast of East Antarctica, all features that are present in the observations [e.g., *Allison*, 1989; *Kottmeier et al.*, 1992; *World Meteorological Organization*, 1994]. The fastest ice is found near the ice edge during winter months, with maximum monthly mean velocities of about 0.2 m s^{-1}.

The geographical distribution of the modeled ice thickness is determined, to a large extent, by the ice drift patterns. In particular, convergent ice motions yield ice buildups of 3–4 m in thickness in the western Weddell Sea, the eastern Bellingshausen Sea, the Amundsen Sea, and the eastern Ross Sea. As can been seen from the March thickness distribution (Figure 5e), the model overestimates the amount of multiyear ice, especially in the eastern Weddell Sea and in the western Ross Sea. Interestingly enough, *Stössel et al.* [1990] obtained the same kind of behavior with a sea ice–mixed layer–pycnocline model using basically the same atmospheric forcing fields as those employed here. Overall, the September ice thickness distribution simulated by the model (Figure 5f) is consistent with the observational estimates (see, for example, *Budd* [1991]). However, we must point out that the model tends to produce thicker ice than observed in the western part of the Southern Ocean and thinner ice than observed in the eastern part.

The stratification of the water column in winter is generally much weaker in the Southern Ocean than in the central Arctic. The model captures well this important feature and simulates mixed layer depths of up to 300 m in the southern Weddell Sea and in the western Ross Sea, where the positive salt fluxes associated with the formation of new ice induce a strong mixing of the upper ocean. During summer, the mixed layer retreats to depths ranging between 20 and 50 m but remains as deep as 300 m in the southern Weddell Sea. As a consequence of this weak hydrostatic stability, F_{wv} takes relatively large annual mean values, with maxima occurring

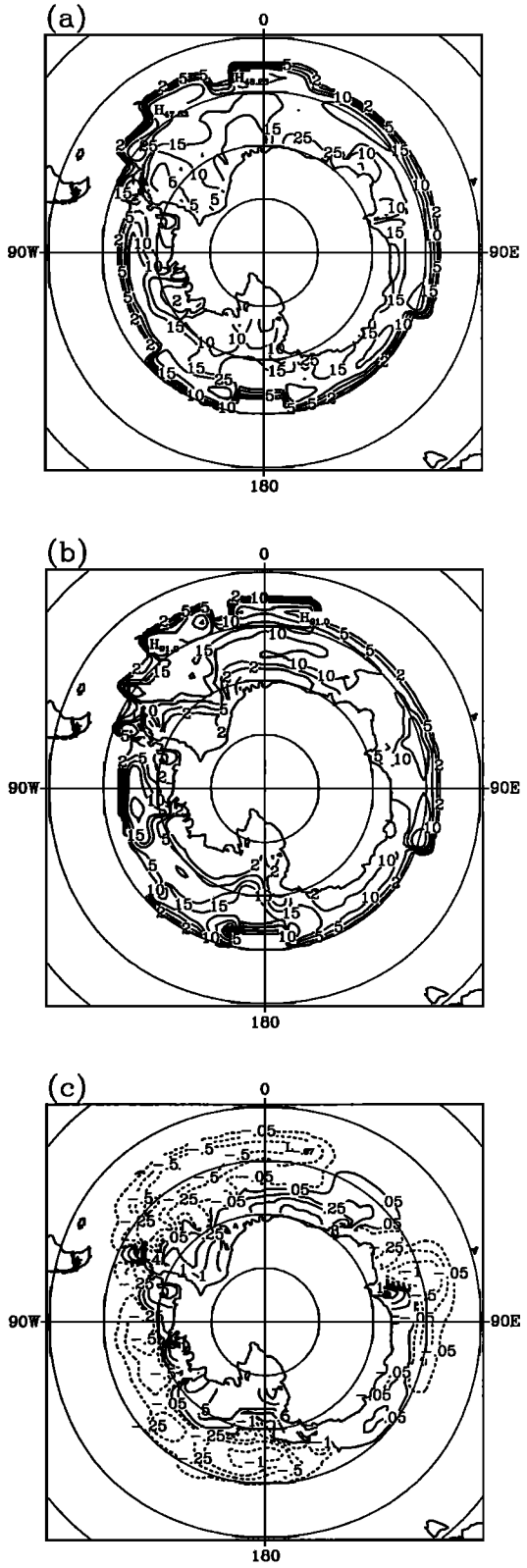

Figure 6. Same as Figure 4, but for the SH.

in regions of net ice production and in the marginal ice zone (Figure 6a). Averaged over the oceanic area covered by ice, this component of the oceanic heat flux is less than 5 W m^{-2} from mid-November to mid-March, but it reaches ~24 W m^{-2} in July, a winter value which falls within the range of current uncertainty (see, for example, *Allison* [1981], *Gordon and Huber* [1990], and *Martinson* [1993]). As expected, F_{wl} (Figure 6b) has a seasonal behavior totally opposite to that of F_{wv}; the average value of this flux is virtually nil during the fall-winter period and attains ~46 W m^{-2} in December. With regard to the net annual ice growth/melt, Figure 6c reveals that the model generates up to 2–3 m of ice per year in several narrow and sparsely located coastal regions, the spatially averaged net ice production amounting to ~0.4 m yr^{-1}. A more uniform net ice melt, averaging ~0.2 m yr^{-1}, takes place at almost all longitudes north of 65°S. As surface ablation in the SH is extremely weak in this simulation, in accordance with the observations [see *Andreas and Ackley*, 1982], this ice melting is almost entirely driven by the large oceanic heat flux at the base of the ice.

Although we have identified a certain number of shortcomings in the results of the control experiment performed with the model, the discussion above demonstrates that the model shows acceptably good agreement with enough aspects of the seasonal behavior of the Arctic and Antarctic ice packs to permit a sound study of its sensitivity to the treatment of ice thermodynamics and dynamics.

4. Sensitivity Experiments

Nine additional experiments (labeled E1 to E9) were carried out in order to evaluate the relative importance of some of the physical processes incorporated in the model. Each experiment consisted of removing a particular parameterization from the standard version of the model and in integrating the degraded model for a 10-year period from the same initial state and under the same forcing conditions as in the control simulation (experiment E0). Table 2 succinctly indicates the change made in the model formulation in each case. The first six experiments concern the vertical growth and decay of the ice (theme 1), the next one concerns the lateral growth and decay of the ice (theme 2), and the last two ones concern the ice dynamics (theme 3).

The extent to which the removal of a given parameterization influences the outcome of the model integration will be basically examined in terms of the equilibrium response of four key variables: the effective ice area A_{eff}; the total ice volume V_i; the net surface heat flux averaged over the entire area occupied by the pack (including leads) $\langle F_{\text{net}} \rangle$; and the oceanic heat flux, excluding the contribution from leads, averaged over the oceanic area covered by ice $\langle F_{wv} \rangle$. To quantify this response, we introduce a couple of sensitivity parameters:

$$\delta_{\Phi}^{\max} = \frac{\Phi^{\max} - \bar{\Phi}^{\max}}{\bar{\Phi}^{\max} - \bar{\Phi}^{\min}} \tag{34}$$

$$\delta_{\Phi}^{\min} = \frac{\Phi^{\min} - \bar{\Phi}^{\min}}{\bar{\Phi}^{\max} - \bar{\Phi}^{\min}} \tag{35}$$

where Φ stands for any of the quantities enumerated above, $\Phi^{\max}$ and $\Phi^{\min}$ are the seasonal upper and lower bounds of Φ in a given experiment, and the overbar denotes a value from the control experiment. Tables 3 to 6 give the seasonal maxima and minima of A_{eff}, V_i, $\langle F_{\text{net}} \rangle$, and $\langle F_{wv} \rangle$, the dates of their occurrence, and the values of $\delta_{\Phi}^{\max}$ and $\delta_{\Phi}^{\min}$ for all the experiments and for both hemispheres.

4.1. Theme 1: Vertical Growth and Decay of the Ice

Leaving aside the effects of ice dynamics, the vertical growth and decay of a well-developed sea ice cover are primarily determined by the way the snow-ice system integrates its top and bottom heat forcings. Two antagonistic processes intervene in this integration. On the one hand, energy is absorbed by the system and stored inside in the form of sensible heat (in the frozen part) and of latent heat (in the brine pockets). On the other hand, energy is transported through and extracted from the system by thermal conduction. Since the specific heats and thermal conductivities of snow and ice differ considerably from each other, the dominance of either of these two competing processes is largely controlled by the relative amounts of snow and ice in the sys-

Table 2. List of Experiments

Name	Description
E0	control simulation
E1	no storage of sensible and latent heat within the snow-ice system (zero-layer model)
E2	no storage of latent heat within the snow-ice system
E3	no penetration of shortwave radiation into the ice
E4	$G(h_e)$ taken equal to unity
E5	no snow
E6	no formation of snow ice
E7	no leads
E8	no ice motion
E9	no shear strength (cavitating fluid rheology)

Table 3. Sensitivity of the Effective Ice Area A_{eff} and Total Ice Volume V_i in the Northern Hemisphere

	A_{eff}						V_i					
Experiment	Max*	$\delta^{\max}_{A_{\text{eff}}}$	Date†	Min*	$\delta^{\min}_{A_{\text{eff}}}$	Date†	Max*	$\delta^{\max}_{V_i}$	Date†	Min*	$\delta^{\min}_{V_i}$	Date†
E0	14.3		68	4.3		250	32.9		121	14.3		259
E1	14.3	0	+0	3.4	−10	−3	29.8	−17	−4	8.6	−30	−8
E2	14.3	0	+0	3.6	−8	−2	30.4	−14	+0	9.8	−24	−7
E3	14.3	0	+0	3.6	−8	−2	30.4	−14	+0	9.8	−24	−7
E4	14.2	−1	−1	3.2	−11	−2	24.8	−44	−5	7.5	−36	−7
E5	14.2	−1	+1	4.3	−1	+1	34.8	10	−5	14.2	−1	+0
E6	14.3	0	+0	4.4	0	+0	32.8	0	+0	14.3	0	+0
E7	14.9	6	+19	5.2	9	+0	25.0	−43	+9	9.6	−25	+6
E8	13.6	−7	+6	4.6	3	−2	36.2	18	+4	21.0	36	−5
E9	14.3	0	+0	4.1	−2	−1	32.4	−3	−1	14.0	−1	−3

See Table 2 for the description of the experiments. The seasonal extrema of A_{eff} and V_i are in 10^6 km^2 and 10^3 km^3, respectively. Values of the sensitivity parameters $\delta^{\max}_{A_{\text{eff}}}$, $\delta^{\min}_{A_{\text{eff}}}$, $\delta^{\max}_{V_i}$, and $\delta^{\max}_{V_i}$ are in percent.

*Max is seasonal maximum and min is seasonal minimum.

†For experiment E0, the days of occurrence of the seasonal extrema of A_{eff} and V_i are given (1 is January 1 and 365 is December 31). For the other experiments, the phase shifts (in days) are given.

tem. A moderately thick snow layer on top of the ice efficiently insulates the latter from the air above while barely contributing to the heat content of the system. This implies that the ice growth in fall and winter will be slower for snow-covered ice than for snow-free ice. However, this insulation effect can be compensated, at least partly, by the decrease in ice ablation during spring and summer caused by the fact that (1) the highly reflective snow cap restricts the solar energy input to the surface, thereby retarding the onset of melting, and (2) this cap has to be melted away before ice begins itself to melt. (Henceforth, this effect will be referred to as the albedo-mass effect.) Snow can further affect the thermodynamic evolution of sea ice through the process of snow ice formation. All these processes constitute the target of the first six sensitivity experiments conducted with the model.

4.1.1. Experiments E1, E2, and E3: Thermal inertia of snow and ice. In experiment E1, the storage of sensible and latent heat within the snow-ice system was not taken into consideration. In practice, this was done by setting the snow and ice specific heats equal to zero and by forcing the solar energy absorbed within the ice to contribute instantaneously to the top surface heat balance. The resulting model must not be confounded with the zero-layer model of *Semtner* [1976]. In the latter, the snow and ice thermal conductivities and the surface albedo are adjusted to

Table 4. Sensitivity of the Net Surface Heat Flux $\langle F_{\text{net}} \rangle$ and Oceanic Heat Flux $\langle F_{wv} \rangle$ in the Northern Hemisphere

	$\langle F_{\text{net}} \rangle$						$\langle F_{wv} \rangle$					
Experiment	Max*	$\delta^{\max}_{\langle F_{\text{net}} \rangle}$	Date†	Min*	$\delta^{\min}_{\langle F_{\text{net}} \rangle}$	Date†	Max*	$\delta^{\max}_{\langle F_{wv} \rangle}$	Date†	Min*	$\delta^{\min}_{\langle F_{wv} \rangle}$	Date†
E0	128.5		192	−72.5		307	22.6		29	1.6		241
E1	132.1	2	+1	−72.5	0	+8	22.6	0	−9	2.4	4	−1
E2	131.5	2	+1	−72.7	0	+9	22.2	−2	−8	2.2	3	+0
E3	131.5	2	+1	−72.7	0	+9	22.1	−2	−7	−0.2	−9	−48
E4	127.8	0	+0	−76.0	−2	−4	23.1	2	−7	2.1	2	+1
E5	129.5	0	−2	−80.1	−4	+0	23.1	2	+11	1.6	0	−6
E6	128.5	0	+0	−72.4	0	+0	22.6	0	+1	1.6	0	−1
E7	116.6	−6	+1	−59.1	7	+4	14.2	−40	−1	1.6	−1	+11
E8	125.8	−1	+2	−71.7	0	+2	16.7	−28	−16	1.1	−3	+0
E9	128.1	0	+0	−73.4	0	+0	23.8	6	−5	1.5	−1	−3

See Table 2 for the description of the experiments. The seasonal extrema of $\langle F_{\text{net}} \rangle$ and $\langle F_{wv} \rangle$ are in watts per square meter. Values of the sensitivity parameters $\delta^{\max}_{\langle F_{\text{net}} \rangle}$, $\delta^{\min}_{\langle F_{\text{net}} \rangle}$, $\delta^{\max}_{\langle F_{wv} \rangle}$, and $\delta^{\min}_{\langle F_{wv} \rangle}$ are in percent.

*Max is seasonal maximum and min is seasonal minimum.

†For experiment E0, the days of occurrence of the seasonal extrema of $\langle F_{\text{net}} \rangle$ and $\langle F_{wv} \rangle$ are given (1 is January 1 and 365 is December 31). For the other experiments, the phase shifts (in days) are given.

Table 5. Sensitivity of the Effective Ice Area A_{eff} and Total Ice Volume V_i in the Southern Hemisphere

	A_{eff}						V_i					
Experiment	Max*	$\delta^{\max}_{A_{\text{eff}}}$	Date†	Min*	$\delta^{\min}_{A_{\text{eff}}}$	Date†	Max*	$\delta^{\max}_{V_i}$	Date†	Min*	$\delta^{\min}_{V_i}$	Date†
E0	17.1		264	4.7		61	21.6		279	9.4		66
E1	17.1	0	+0	4.6	−1	+0	21.4	−1	+0	9.1	−2	−1
E2	17.1	0	+0	4.7	0	+0	21.5	0	+1	9.3	−1	+0
E3	17.1	0	+0	4.7	0	+0	21.5	−1	+1	9.3	−1	+0
E4	17.0	−1	−1	4.2	−4	−2	19.0	−21	−1	7.4	−16	−3
E5	17.0	−1	+0	4.1	−5	−9	23.7	18	−2	8.8	−5	−2
E6	17.1	−1	+1	4.9	2	+1	19.3	−18	−3	8.2	−10	+1
E7	18.5	11	−4	7.7	24	+7	13.8	−64	+15	6.9	−20	−1
E8	16.5	−5	+6	5.6	7	+17	35.4	114	+9	25.2	130	+5
E9	17.2	0	+0	4.5	−2	+2	21.0	−5	−1	8.7	−6	+0

See Table 2 for the description of the experiments. The seasonal extrema of A_{eff} and V_i are in 10^6 km^2 and 10^3 km^3, respectively. Values of the sensitivity parameters $\delta^{\max}_{A_{\text{eff}}}$, $\delta^{\min}_{A_{\text{eff}}}$, $\delta^{\max}_{V_i}$, and $\delta^{\max}_{V_i}$ are in percent.

*Max is seasonal maximum and min is seasonal minimum.

†For experiment E0, the days of occurrence of the seasonal extrema of A_{eff} and V_i are given (1 is January 1 and 365 is December 31). For the other experiments, the phase shifts (in days) are given.

compensate for the error in annual mean ice thickness arising from the neglect of heat storage. Although such a tuning is deemed fairly acceptable in the case of a stand-alone sea ice model, it is liable to introduce artificial perturbations in the surface energy balance that could have serious consequences if the sea ice model is incorporated into an AOGCM. In experiment E2, only the storage of latent heat in the brine pockets was ignored. (It does not make much sense to perform the corresponding experiment for the storage of sensible heat. In such an experiment, the heat capacity of the snow-ice system would be zero and, consequently, the heat accumulated in the brine reservoir during summer could not be used to moderate the ice cooling in autumn. This energy could always be applied directly at the bottom of the ice slab to delay the onset of the ice growth. However, this way of doing would involve an important alteration in the model physics.) Usually, the effect of the brine pockets is evaluated by setting equal to zero the parameter i_0, i.e., by preventing the shortwave radiation from penetrating inside the ice [*Maykut and Untersteiner*, 1971; *Semtner*, 1976]. This practice does not allow one to isolate properly the influence of brine pockets when using a coupled ice-ocean model, as it is the case here, because the shortwave energy input into the under-ice mixed layer, which itself contributes to the oceanic heat flux, is modified at the same time. Nevertheless, to assess the difference between this procedure and the one followed in experiment E2, we performed a third experiment (E3) with $i_0 = 0$.

Table 6. Sensitivity of the Net Surface Heat Flux $\langle F_{\text{net}} \rangle$ and Oceanic Heat Flux $\langle F_{wv} \rangle$ in the Southern Hemisphere

	$\langle F_{\text{net}} \rangle$						$\langle F_{wv} \rangle$					
Experiment	Max*	$\delta^{\max}_{\langle F_{\text{net}} \rangle}$	Date†	Min*	$\delta^{\min}_{\langle F_{\text{net}} \rangle}$	Date†	Max*	$\delta^{\max}_{\langle F_{wv} \rangle}$	Date†	Min*	$\delta^{\min}_{\langle F_{wv} \rangle}$	Date†
E0	77.1		361	−54.0		139	23.6		190	1.5		355
E1	77.3	0	+0	−54.5	0	+0	23.9	2	−3	1.4	0	+0
E2	77.4	0	+0	−54.0	0	+0	23.6	0	−3	1.5	0	+2
E3	77.1	0	+0	−54.1	0	+0	23.7	1	−2	0.7	−3	+11
E4	73.6	−3	+0	−57.3	−3	+0	27.9	20	+2	1.7	1	−7
E5	87.0	8	−7	−66.4	−10	−3	26.8	15	+4	4.8	15	+27
E6	71.3	−4	+0	−52.6	1	+1	23.9	2	−10	1.4	0	+4
E7	53.3	−18	+4	−34.9	15	+3	15.0	−39	+4	2.6	5	−5
E8	64.2	−10	+1	−43.3	8	+7	18.3	−24	+5	2.9	7	+71
E9	77.7	0	−2	−55.0	−1	−1	24.2	3	+0	1.6	1	+0

See Table 2 for the description of the experiments. The seasonal extrema of $\langle F_{\text{net}} \rangle$ and $\langle F_{wv} \rangle$ are in watts per square meter. Values of the sensitivity parameters $\delta^{\max}_{\langle F_{\text{net}} \rangle}$, $\delta^{\min}_{\langle F_{\text{net}} \rangle}$, $\delta^{\max}_{\langle F_{wv} \rangle}$, and $\delta^{\min}_{\langle F_{wv} \rangle}$ are in percent.

*Max is seasonal maximum and min is seasonal minimum.

†For experiment E0, the days of occurrence of the seasonal extrema of $\langle F_{\text{net}} \rangle$ and $\langle F_{wv} \rangle$ are given (1 is January 1 and 365 is December 31). For the other experiments, the phase shifts (in days) are given.

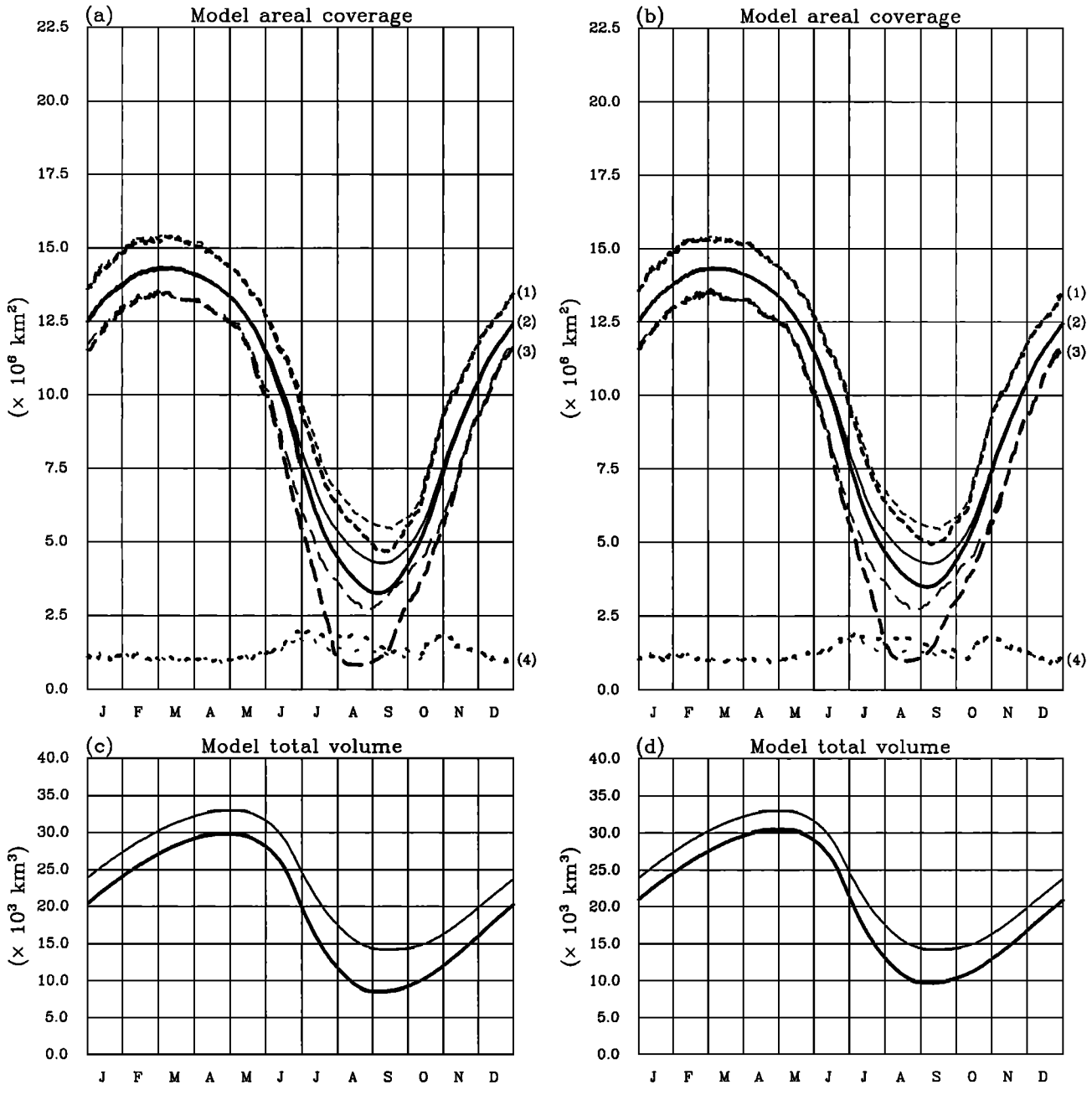

Figure 7. (a) Seasonal cycles of ice extent (curves labeled 1), effective ice area (curves labeled 2), ice area at the 85% concentration (curves labeled 3), and open water area (curves labeled 4) in the NH from experiments E1 (thick curves) and E0 (thin curves). (b) Same as Figure 7a, except for experiments E2 and E0. (c) Seasonal cycles of total ice volume in the NH from experiments E1 (thick curve) and E0 (thin curve). (d) Same as Figure 7c, except for experiments E2 and E0.

In the central Arctic, the observed ice thickness is typically 3 m and the seasonal range of the vertically averaged temperature of the ice is roughly 10°C (see *Maykut and Untersteiner* [1971, Figure 3], who show the observed temperature and thickness of perennial sea ice at International Geophysical Year Station Alpha, 1957–1958). From this, we can estimate that the year-round variation of the ice sensible heat content, at a constant ice thickness, corresponds to an annual mean heat flux of ~1.8 W m^{-2}. With regard to the storage of latent heat, let us assume a June-to-July average net shortwave radiation of 64 W m^{-2} [*Maykut and Untersteiner*, 1971, Table 2] and a value of 0.3 for i_0 (which corresponds to a cloud fraction of 0.8). Since nearly all the penetrating solar energy is trapped inside the ice, these numbers lead to an equivalent annual mean heat flux of ~4.8 W m^{-2}. This back-of-the-envelope calculation (which ignores a number of important effects, like those associated with ice dynamics) suggests that the storage of latent (sensible) heat accounts for ~70% (~30%) of

the seasonal variation of the total heat content of thick ice in the Arctic.

Figures 7a and 7b depict the seasonal cycles of the ice extent, the effective ice area, the ice area at the 85% concentration, and the open water area in the NH for experiments E1 and E2, respectively. From midautumn to late spring, the ice areal coverage is scarcely sensitive to the omission of the snow-ice thermal inertia. Once the snow cover has totally disappeared (i.e., in late June), the ice cover in either of the two experiments begins to shrink at a rate greater than in experiment E0, leading to a moderate decrease of the minimum ice extent and to a significant reduction of the minimum effective ice area. As for the ice area at the 85% concentration, it undergoes a strong decrease during summer. The fact that the ice area becomes more responsive as the cutoff concentration A_c increases is circumstantial evidence that we are dealing here with phenomena that mainly touch the thickest ice in the basin. There is no wonder in this since the ice thermal inertia depends linearly on the ice volume. Also of note is that the fraction of open water in both experiments is larger than in experiment E0 by ~0.1 from July to September.

As in the case of the ice areal coverage, the total ice volume at the height of the melting period is much smaller in experiments E1 and E2 (Figures 7c and 7d, respectively) than in experiment E0. However, while the ice area quickly catches up to the control simulation values once freezing begins, the difference in volume is maintained, although somewhat mitigated, during the whole seasonal cycle. Essentially, the modified initial conditions (lower ice volume in summer) for the subsequent fall and winter seasons are such that the enhanced growth rate associated with the thinner ice cannot compensate for the summer reduction. The average ice thickness $\langle h_i \rangle$ in experiment E1 differs from the one in the control case by about −0.1 m in March and by as much as −0.8 m in August and September. In experiment E2, the difference amounts approximately to −0.1 m in March and to −0.6 m in August and September. Clearly, the brine damping mechanism plays a crucial role in determining the seasonal evolution of the ice pack in the model NH. When this process is removed from the model (experiment E2), more energy becomes available for melting at the surface and, in consequence, the equilibrium ice thickness decreases noticeably (Figure 8a). Further eliminating the contribution of the sensible heat storage (experiment E1) yields a slightly enhanced reduction of thickness in the central Arctic and in the Greenland Sea, where the thickest ice is encountered (Figure 8b).

Semtner [1984] conducted a series of experiments with his three-layer and zero-layer thermodynamic sea ice models in order to compare their performance under the atmospheric and oceanic conditions that prevail in the central Arctic. He showed that the amplitude of the seasonal cycle of ice thickness is exaggerated when the storage of sensible and latent heat is neglected. Moreover, he found a substantial phase error (1 month lead) on the part of the zero-layer model in predicting both the onset of melting in spring and the commencement of ice growth in fall. The phase lead in spring was attributed to the neglect of the heat capacity of the system, while that in autumn was imputed to the absence of latent heat storage. We have to emphasize that these results were obtained with a one-dimensional model that ignores the moderating effects of ice dynamics (see *Lemke et al.* [1990] for a discussion of these effects). The dates of occurrence of the maximum and minimum ice volumes predicted by our model in the NH have a much weaker sensitivity to the omission of the thermal inertia of snow and ice than that reported by *Semtner* [1984, Table 3]. The maximum ice volume in experiment E1 precedes the maximum in the control simulation by about half a week and the phase lead of

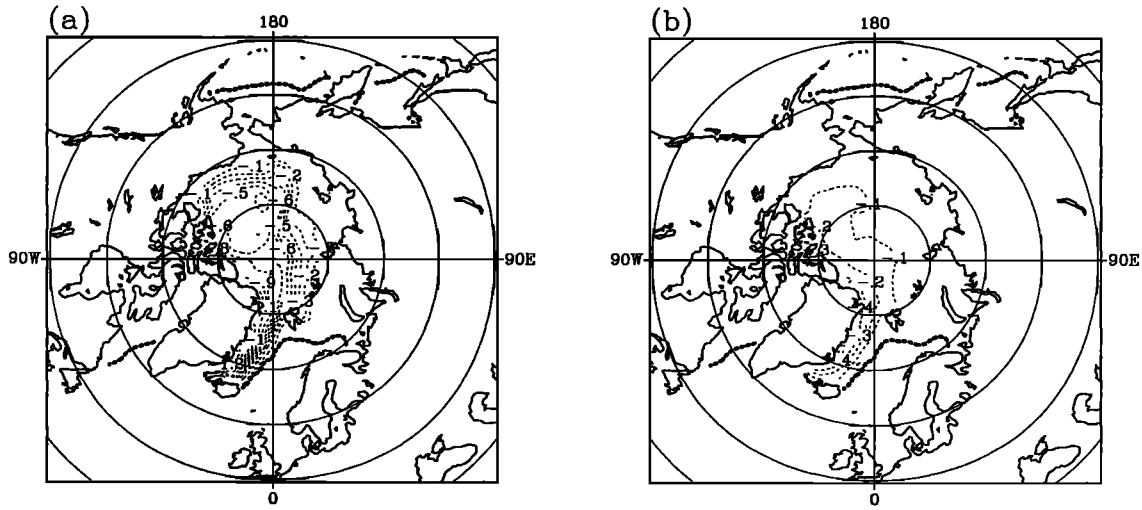

Figure 8. Geographical distribution of the difference in annual mean ice thickness over the Arctic Ocean and peripheral seas (a) between experiments E2 and E0 and (b) between experiments E1 and E2. The contour interval is 0.1 m. The thick, stippled line represents the 0.1 m ice thickness contour from experiment E0.

the minimum ice volume is of only $1\frac{1}{2}$ weeks. In contrast, the shifts in the dates of occurrence of the seasonal extrema of the average ice thickness, which contain a stronger signal from the massive central pack, are much larger. The maximum of $\langle h_i \rangle$ in experiment E1 (E2) takes place 6 weeks (5 weeks) earlier than in experiment E0 and is ~0.7 m (~0.5 m) smaller. The corresponding numbers for the minimum of $\langle h_i \rangle$ are 2 weeks ($1\frac{1}{2}$ weeks) and ~0.4 m (~0.3 m).

The sole difference between experiments E2 and E3 lies in the disposition of solar energy within the sea ice and the upper ocean. Whereas an amount of shortwave radiation F_{str} is transmitted through bare ice into the mixed layer in experiment E2, all the nonreflected shortwave radiation is absorbed at the ice surface in experiment E3. Recalling that the solar radiation passing through ice is one of the model sources of oceanic heat flux, the response of F_{wv} is expected to differ in experiments E2 and E3, particularly in regions of relatively thin ice. This is actually the case. Experiment E3 yields values of $\langle F_{wv} \rangle$ that from June to August are 2 to 3 W m^{-2} smaller than in experiment E2. Furthermore, Table 4 indicates that the minimum of $\langle F_{wv} \rangle$ in experiment E3 precedes the one in experiment E2 by about 7 weeks. It is interesting to note that the summer deficit in F_{wv} simulated in experiment E3 as compared to experiment E2 has no consequence whatsoever on the overall ice melting. The solar energy absorbed by the ice-ocean system is merely distributed differently than in experiment E2 so as to favor surface melting at the expense of bottom ablation. As a consequence, the seasonal cycles of the NH ice areal coverage and total ice volume in experiment E3 (not shown) are approximately the same as in experiment E2. It should be noted, however, that the model sensitivity in experiment E3 relative to experiment E2 could be accentuated by the inclusion in the model formulation of processes such as, for example, the formation of surface melt ponds and the changes in salinity with depth in sea ice. The annual mean value of $\langle h_i \rangle$ in experiment E3 is about 0.4 m smaller than in experiment E0, a response that matches almost perfectly those reported by *Maykut and Untersteiner* [1971] and *Semtner* [1976] in similar experiments. We stress, however, that these authors used one-dimensional sea ice models suited for central Arctic conditions, prescribed the turbulent heat fluxes at the surface, and employed a constant value of 0.17 for i_0.

Of particular interest is that the model Antarctic ice pack is quasi-insensitive to the neglect of the snow-ice thermal inertia (see Table 5). This arises from the fact that the Antarctic ice is, for the most part, seasonal (and thus relatively thin) and perennially snow covered.

4.1.2. Experiment E4: Heat conduction. Experiment E4 consisted of setting the conduction correction factor $G(h_e)$ (see (1)) equal to unity. We recall that this factor was introduced in order to implicitly include a variety of snow and ice thicknesses in the treatment of vertical growth and melt and that its value is determined by assuming uniform snow and ice thickness distributions.

The seasonal cycles of the NH and SH ice areal coverages for this experiment are shown in Figures 9a and 9b, respectively. At the end of the melting period, the effective ice area is reduced with respect to the one in experiment E0 by $\sim 1 \times 10^6$ km^2 in the NH and by $\sim 0.5 \times 10^6$ km^2 in the SH. This reduction is linked to the generalized decrease in ice thickness that results from the smaller thermal conductivity of the snow-ice system. The ice being thinner, it is prone to disappear more easily during summer months. The tendency to generate a smaller ice area is not maintained during the cold season. In each hemisphere, the effective ice area almost fully recovers from the enhanced summer melting by midautumn and follows subsequently an evolution close to that in the control simulation. This weak sensitivity in fall and winter is not surprising since the winter advance of both ice packs takes place basically by freezing of open water. The average ice concentration within the pack $\langle A \rangle$ responds quite similarly, with minor changes during the cold season and an appreciable decrease (up to ~0.1 in the NH and ~0.03 in the SH) in late summer and early fall.

The lowering of the thermal conductivity is conducive to a slowdown of the vertical ice growth (without much changing the melting rate) and hence to a decrease in ice volume (Figures 9c and 9d). While as mentioned above, the largest response of the ice area occurs in late summer, the total ice volume is more responsive in late winter and in spring. The reduction of V_i in the NH (SH) amounts to $\sim 8 \times 10^3$ km^3 ($\sim 2.5 \times 10^3$ km^3) at the time of the seasonal maximum and to $\sim 7 \times 10^3$ km^3 ($\sim 2 \times 10^3$ km^3) at the time of the minimum. On an annual average, the ice cover in the NH (SH) undergoes a decrease of about 30% (20%) in volume. The somewhat more moderate response in the SH is a consequence of the relative thinness of the Antarctic sea ice. In both hemispheres, the main contribution to this drastic reduction of ice volume comes from the regions of thick ice, i.e., the central Arctic and the Greenland Sea in the NH (Figure 10a) and the western sector of the Southern Ocean in the SH (Figure 10b). It should be noted here that as the ice volume decreases, there is a concomitant reduction in the sensible and latent heat content of the pack, which tends to amplify the initial decrease. The signature of the lesser thermal inertia is apparent in the dates of occurrence of the maximum and minimum ice thicknesses in the NH. The maximum (minimum) of $\langle h_i \rangle$ is approximately 1 m (0.6 m) smaller than in experiment E0 and takes place almost 10 (6) weeks in advance. In the SH, $\langle h_i \rangle$ is about 0.2 m smaller than in the control simulation all year long and its extrema experience no noticeable phase shift.

Tables 4 and 6 reveal that the seasonal ranges of $\langle F_{\text{net}} \rangle$ and $\langle F_{wv} \rangle$ differ slightly from those generated in experiment E0. As a result of the larger percentage of open water during late summer and early fall, the surface heat losses associated with the outgoing longwave radiation and turbulent heat fluxes are significantly larger during this period, which gives rise to monthly mean values of $\langle F_{\text{net}} \rangle$ that are smaller than

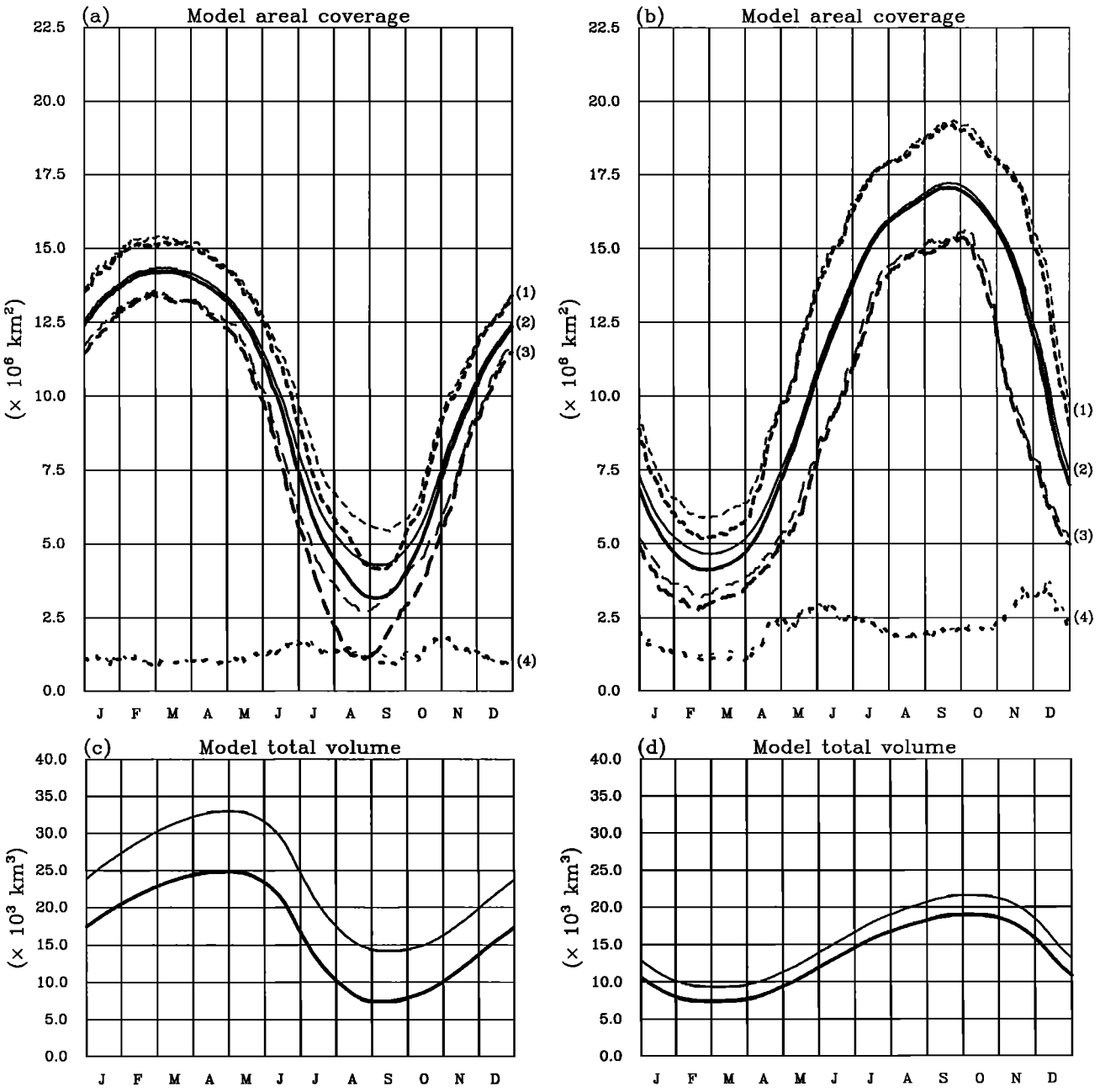

Figure 9. (a) Seasonal cycles of ice extent (curves labeled 1), effective ice area (curves labeled 2), ice area at the 85% concentration (curves labeled 3), and open water area (curves labeled 4) in the NH from experiments E4 (thick curves) and E0 (thin curves). (b) Same as Figure 9a, except for the SH. (c) Seasonal cycles of total ice volume in the NH from experiments E4 (thick curve) and E0 (thin curve). (d) Same as Figure 9c, except for the SH.

those in the control case by as much as ~7 W m^{-2} in the NH (September) and ~4 W m^{-2} in the SH (March). As autumn progresses, leads close and owing to the reduced thermal conductivity, the surface of the snow-ice system becomes colder than in experiment E0. The surface temperature averaged over the whole area occupied by the pack (including leads) $\langle T_s \rangle$ drops by about 1°C from January to March in the NH and by about 0.5°C from August to September in the SH. This cooling limits the radiative and turbulent heat losses of the pack, leading to an average increase in $\langle F_{net} \rangle$ of ~5 W m^{-2} in the NH and of ~3 W m^{-2} in the SH.

Hibler [1984] and *Harvey* [1988] studied the effect of the inclusion of an uniform ice thickness distribution on the performance of their respective models. Although they used a somewhat more elaborate scheme than the one proposed here (they selected a number of thickness categories and computed the thermodynamic growth/melt rate of each category separately), they obtained a response which is, in many respects, similar to

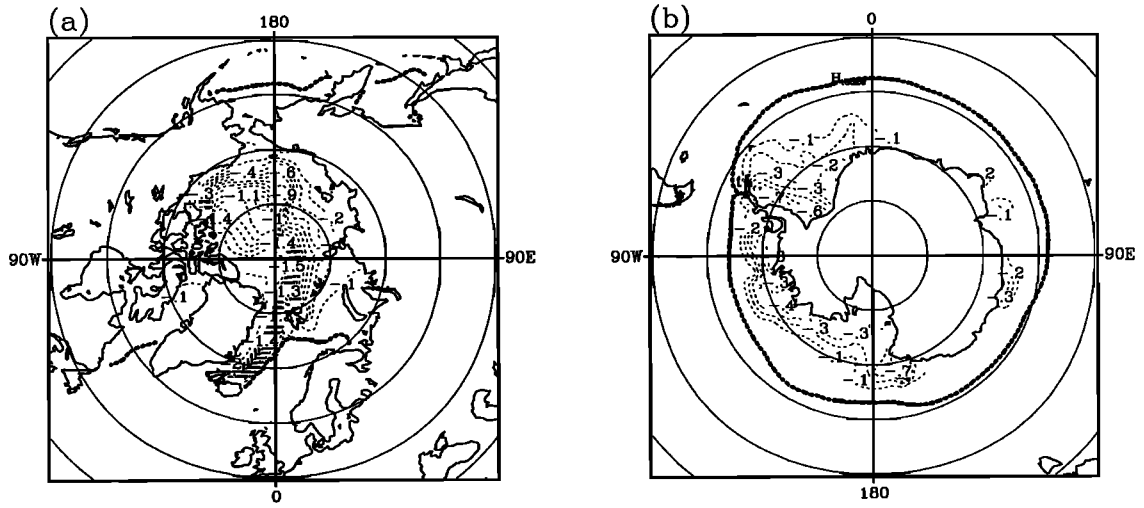

Figure 10. Geographical distribution of the difference in annual mean ice thickness between experiments E4 and E0 (a) over the Arctic Ocean and peripheral seas and (b) over the Southern Ocean. The contour interval is 0.1 m. The thick, stippled line represents the 0.1 m ice thickness contour from experiment E0.

ours. Our results are also consistent with those of *Hibler* [1992]. This author compared the behaviors of his two-level model [*Hibler*, 1979] and full multilevel model [*Hibler*, 1980] in the NH and found that the multilevel approach yields an increase in overall thickness whose magnitude is of the order of the one reported here.

4.1.3. Experiments E5 and E6: Snow cover. A number of modeling studies [*Maykut and Untersteiner*, 1971; *Semtner*, 1976; *Harvey*, 1988; *Ledley*, 1991, 1993; *Holland et al.*, 1993; *Ebert and Curry*, 1993] suggest that annual snowfall rates less than about twice the observed value have only a modest influence on the equilibrium ice thickness in the Arctic. This relative insensitivity arises from the fact that the two antagonistic effects mentioned previously (namely, the insulation effect and the albedo-mass effect) tend to offset each other. By contrast, the numerical experiments carried out by *Owens and Lemke* [1990] and *Stössel et al.* [1990] suggest that the Antarctic sea ice is remarkably sensitive to the presence or absence of snow and that the insulation effect dominates the influence of the albedo and mass in the SH. The authors attributed this difference of behavior to the fact that the ratio of snow thickness to ice thickness is much larger in the SH than in the NH. However, it is worth pointing out that their models did not take account snow ice formation, a process that seems to play an important part in shaping the seasonal cycles of the snow and ice thicknesses in the SH [see *Eicken et al.*, 1995]. This conversion of snow into ice, if any, might counteract, to some extent, the strong decrease in the freezing rate related to the presence of a highly insulating snow layer. Two experiments were performed with our model in order to assess how and to what degree snow and snow ice formation affect the characteristics of both ice packs. In the first one (E5), snow depths were initialized to zero and snow was not allowed to accumulate on top of the ice (snow falling over the ice-covered portion of a grid cell was immediately transferred into leads), whereas in the second one (E6), the scheme of snow ice formation was not activated.

Figure 11a indicates that for snowfall rates typical of the present-day climate, the absence of snow accumulation on sea ice has little effect on the seasonal cycle of the ice areal coverage in the model NH. As can be seen from Figure 11b, the SH ice cover is more sensitive to the perturbation. The response, however, is restricted to the period extending from November to May, during which the effective ice area and the open water area are, on average, about 1×10^6 km^2 smaller and 0.5×10^6 km^2 greater than in experiment E0, respectively. This reduction of ice coverage during the warm season is primarily a consequence of the decrease in albedo and of the suppression of the snow mass effect. Note that this result contradicts the findings of *Owens and Lemke* [1990] and *Stössel et al.* [1990], who obtained in their respective simulations of the Weddell Sea ice cover and entire Antarctic ice pack a larger ice extent throughout the year when snow was omitted. The more pronounced sensitivity observed in the SH as compared to that in the NH derives from the fact that the Antarctic sea ice in the control simulation is continuously covered by a thick snow layer (which results from the relatively intense snowfalls that prevail over the Southern Ocean and from the near total absence of surface ablation), while the Arctic one becomes completely free of snow in summertime.

During winter and spring, the total ice volume undergoes an increase of approximately the same magnitude in both hemispheres (Figures 11c and 11d). In fact, the absence of snow allows a stronger cooling of the ice during the cold season, which stimulates heat conduction and hence basal accretion. In the SH, V_i takes slightly smaller values than in experiment E0 between

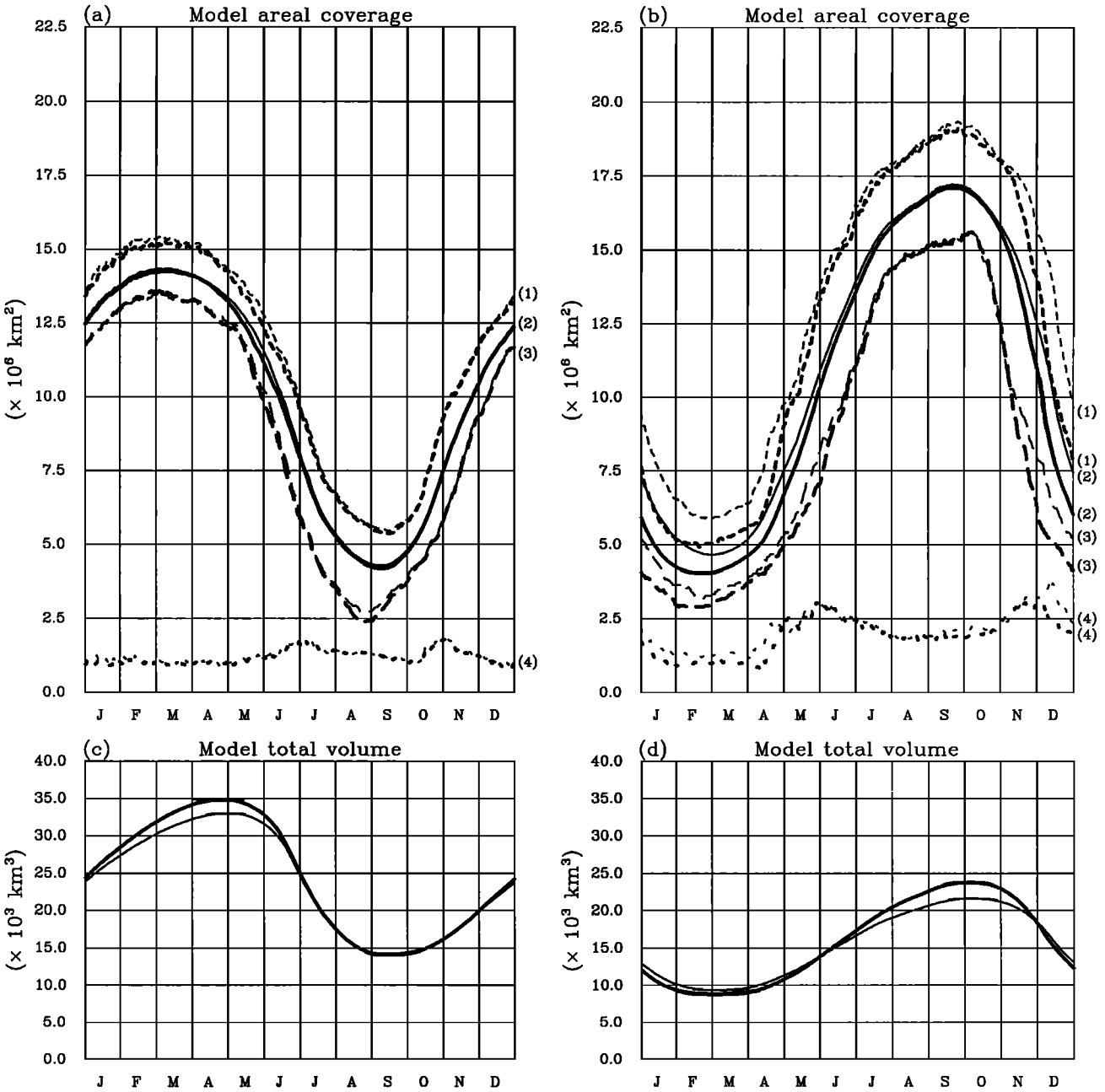

Figure 11. (a) Seasonal cycles of ice extent (curves labeled 1), effective ice area (curves labeled 2), ice area at the 85% concentration (curves labeled 3), and open water area (curves labeled 4) in the NH from experiments E5 (thick curves) and E0 (thin curves). (b) Same as Figure 11a, except for the SH. (c) Seasonal cycles of total ice volume in the NH from experiments E5 (thick curve) and E0 (thin curve). (d) Same as Figure 11c, except for the SH.

December and May. A number of factors intervene in determining this negative response: (1) the albedo decrease (the surface albedo is, on average, ~0.1 lower than in the control simulation) and the fact that there is no snow to melt (two factors that promote the ablation of the ice at its top surface); (2) the transmission of shortwave radiation through ice into the underlying mixed layer, which increases the oceanic heat flux and thus the basal melting; and (3) the absence of snow ice formation, which in experiment E0 contributes to the thickening of the ice from late summer to midspring. Here $\langle h_i \rangle$ is not much affected by the perturbation, its annual mean value being only ~0.1 m higher in the NH and ~0.15 m higher in the SH. However, we shall see later on that the geographical distribution of the ice thickness in the SH is noticeably altered.

Tables 4 and 6 show that neglecting the presence of snow has a pronounced effect on the seasonal cycle of $\langle F_{net} \rangle$ in both hemispheres. Being devoid of its protective snow blanket, sea ice experiences a more severe cooling in fall and winter; but owing also to the absence of snow, the surface in contact with the atmosphere is

appreciably warmer during these seasons, which causes an increase in the outgoing longwave radiation and latent heat flux and a decrease in the sensible heat flux (the latter two fluxes are upward and downward, respectively, over sea ice during most of the cold months). As a matter of fact, $\langle T_s \rangle$ is up to ~1°C higher in both hemispheres during the fall-winter period, leading to NH and SH values of $\langle F_{net} \rangle$ that are, on average, ~7 and ~10 W m^{-2} smaller, respectively. The response becomes positive in spring. Because of the reduction in albedo, the net shortwave radiation increases markedly during this season, yielding a net heat gain at the surface that is larger with respect to that in the control case by ~9 W m^{-2} in the NH and by ~14 W m^{-2} in the SH, on average. While the seasonal behavior of $\langle F_{wv} \rangle$ is virtually unaffected by the removal of the snow cover in the NH (see Table 4), it undergoes a major change in the SH (see Table 6). During autumn and winter, the stronger ice accretion leads to an enhanced rejection of brine into the mixed layer, which intensifies the vertical mixing. A greater amount of relatively warm pycnocline water is therefore entrained into the mixed layer and, consequently, the oceanic heat flux increases (from May to August, $\langle F_{wv} \rangle$ is higher than in experiment E0 by 3 to 4 W m^{-2}). On the other hand, in the absence of snow cap, an extra energy flux enters the under-ice mixed layer of the Southern Ocean in spring and summer, namely, the solar radiation transmitted through ice. This surplus of energy induces an increase in $\langle F_{wv} \rangle$ that reaches about 7 W m^{-2} in late spring–early summer.

The combination of relatively small snow depths and large ice thicknesses makes episodes of snow ice formation extremely rare in the model NH; in the control simulation, snow ice is found, in small quantity, only around Spitsbergen between March and May. On the contrary, the snow thickness is comparable to the ice thickness in many regions of the model Southern Ocean, so that snow ice is relatively common there. In experiment E0, snow ice forms from late February–early March to late November in the SH. The overall contribution of meteoric ice (snow ice) to the annual mean total ice volume amounts to ~5.5% (~15%); roughly 7.5% (20%) of the simulated multiyear ice is, in fact, made of meteoric ice (snow ice). These figures are fairly consistent with estimates from the sparse field observations conducted in the Weddell Sea [*Lange et al.*, 1990; *Eicken et al.*, 1994] and in the Ross, Amundsen, and Bellinghausen Seas [*Jeffries et al.*, 1994]. When the process of snow ice formation is not taken into consideration, the snow depth augments at the expense of the ice thickness. The decrease in ice thickness tends to be amplified by the enhancement of the thermal insulation that results from the thickening of the snow cover. However, this effect is counterbalanced, at least partially, by the intensification of the basal ice growth arising from the suppression of the heat input associated with the infiltration of seawater at the freezing point into the snow layer. The seasonal cycles of the SH ice areal coverage and total ice volume as simulated in experiment E6 are illustrated in Figures 12a and 12b, respectively. One

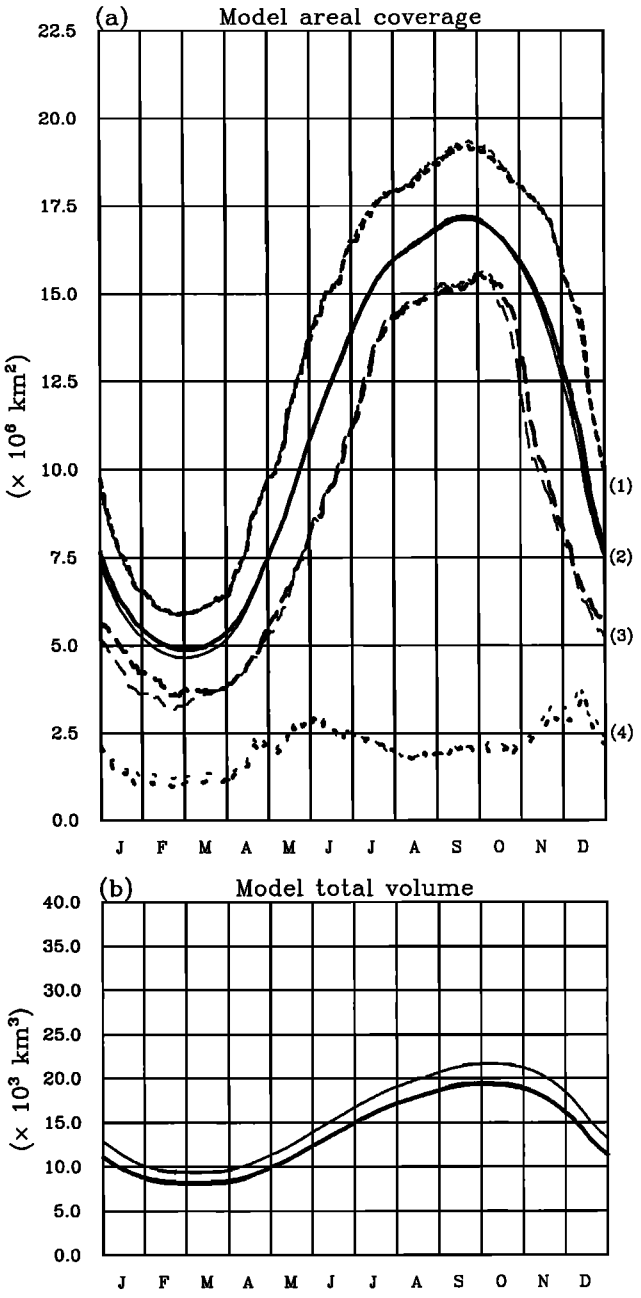

Figure 12. (a) Seasonal cycles of ice extent (curves labeled 1), effective ice area (curves labeled 2), ice area at the 85% concentration (curves labeled 3), and open water area (curves labeled 4) in the SH from experiments E6 (thick curves) and E0 (thin curves). (b) Seasonal cycles of total ice volume in the SH from experiments E6 (thick curve) and E0 (thin curve).

notices a slight increase in the ice area at the 85% concentration throughout the retrait phase and a decrease in ice volume that ranges from ~1 × 10^3 km^3 at the seasonal minimum to ~2.5 × 10^3 km^3 at the seasonal maximum. With regard to $\langle h_i \rangle$, its annual mean value is reduced by about 0.2 m.

Figures 13a and 13b display the changes of annual mean ice thickness in the SH for experiments E5 and E6, respectively. Whatever the experiment, the largest

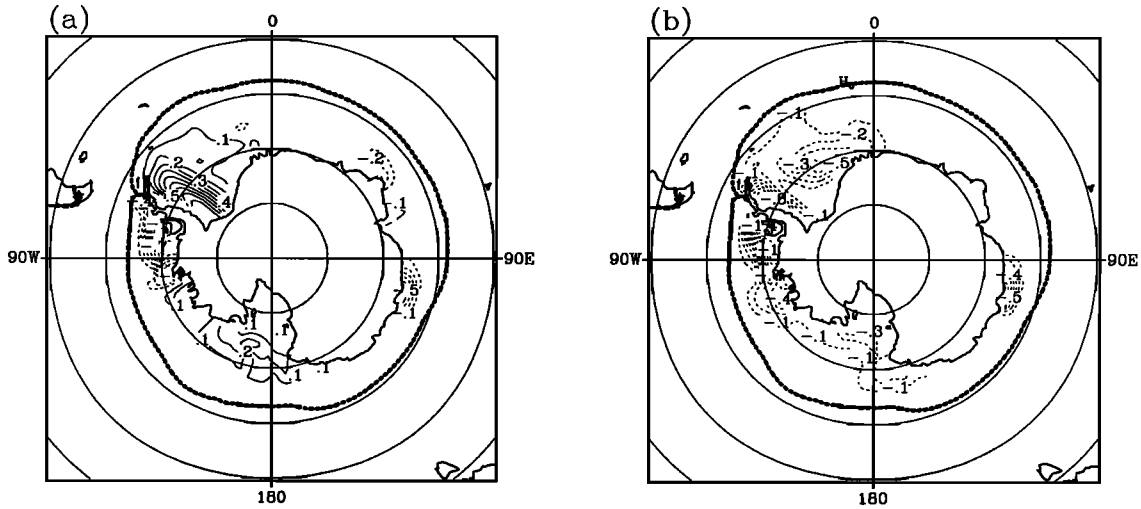

Figure 13. Geographical distribution of the difference in annual mean ice thickness over the Arctic Ocean and peripheral seas (a) between experiments E5 and E0 and (b) between experiments E6 and E0. The contour interval is 0.1 m. The thick, stippled line represents the 0.1 m ice thickness contour from experiment E0.

changes take place in the western sector of the Southern Ocean, where most of the Antarctic multiyear ice resides and the greatest snow depths are encountered. When snow accumulation is not permitted, sea ice thickens in the western Weddell Sea, in the Amundsen Sea, and in the Ross Sea, whereas it gets thinner in the Bellingshausen Sea and in the Indian and western Pacific sectors of the Southern Ocean. If only snow ice formation is switched off, the ice thickness diminishes or remains unchanged in each of these areas. These results indicate that the relative importance of the different effects associated with the snow cover (i.e., the insulation effect, the albedo-mass effect, and the snow ice formation) varies significantly from one region to another in the SH. In the Weddell, Amundsen, and Ross Seas, the insulation effect and snow ice formation compete with one another, but the former effect generally prevails. In the Bellingshausen and western Pacific sector of the Southern Ocean, snow ice formation is the dominant process. Finally, in the Indian sector, the predominant effect is that related to the albedo and mass of snow.

4.2. Theme 2: Lateral Growth and Decay of the Ice

It is generally acknowledged that the existence of leads and polynyas within the ice cover greatly affects the air-ice-ocean interactions. During winter, the turbulent heat loss to the atmosphere, the rate of ice growth, and the salt rejection to the ocean depend strongly on ice thickness, being up to 2 orders of magnitude larger over a refreezing lead or polynya than over the surrounding snow-covered pack ice [*Maykut*, 1982]. During summer, leads and polynyas admit large quantities of shortwave radiation to the upper ocean, which ultimately impact on the mass balance of the ice pack (see, for example, *Maykut and Perovich* [1987] and *Maykut and McPhee* [1995]). Leads and polynyas also modify the surface freshwater and momentum balances since they allow a fraction of the falling snow to reach the ocean, enhance the average evaporation rate, and put the mixed layer in direct contact with the surface winds. In order to evaluate the influence of these areas of open water on the seasonal waxing and waning of the Arctic and Antarctic ice covers, we conducted an experiment (E7) in which the ice concentration was forced to keep a constant value of one wherever ice was present. In order to ensure that mass was conserved in the experiment, the following modifications were made to the code: (1) the advection of ice concentration was switched off; (2) in grids containing ice, both lateral accretion and ablation were not activated; and (3) when ice started growing in a initially ice free grid cell, its thickness was determined by assuming that the volume of ice was distributed uniformly over the entire grid (in experiment E0, the newly formed ice had a specified thickness h_0).

The seasonal cycles of the NH and SH ice areal coverages for this experiment are illustrated in Figures 14a and 14b, respectively. Of course, all the ice area curves coincide and the amount of open water is consistently nil. It can be seen that the effective ice area is much larger than in experiment E0 all year long in both hemispheres. While the NH ice extent is not much affected by the absence of leads, the SH one experiences a pronounced increase during the melting period. This difference of behavior is attributable to the different nature of the processes governing the seasonal swing of the Arctic and Antarctic ice extents in the model. During the fall-winter period, the two packs expand equatorward, mainly as a result of the freezing of the open waters contiguous to the ice edge. From this, we can conclude that the advance of the ice must not depend critically on the amount of open water within the ice-ocean boundary neither in the NH nor in the SH. On

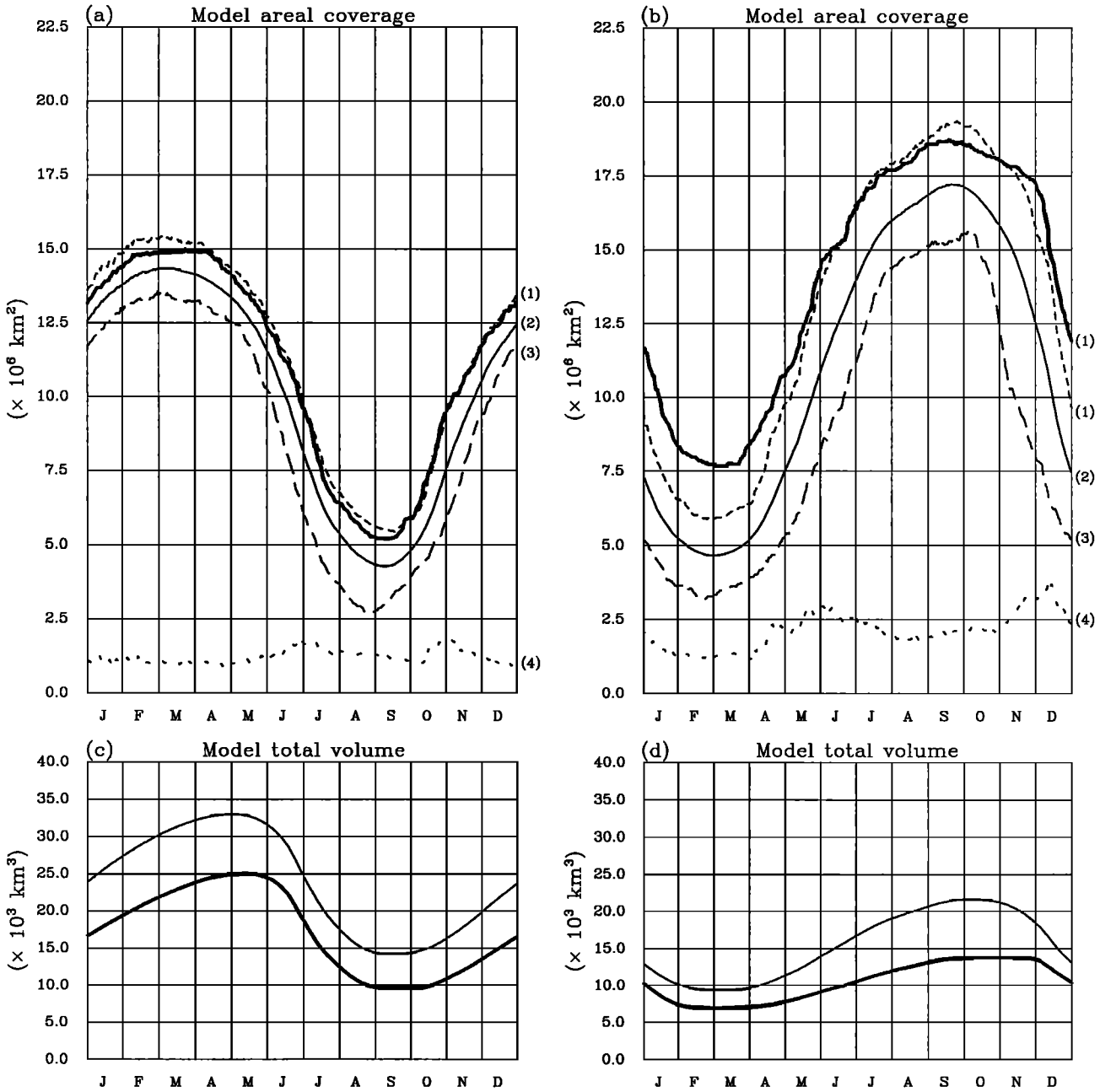

Figure 14. (a) Seasonal cycles of ice extent (curves labeled 1), effective ice area (curves labeled 2), ice area at the 85% concentration (curves labeled 3), and open water area (curves labeled 4) in the NH from experiments E7 (thick curves) and E0 (thin curves). (b) Same as Figure 14a, except for the SH. (c) Seasonal cycles of total ice volume in the NH from experiments E7 (thick curve) and E0 (thin curve). (d) Same as Figure 14c, except for the SH.

the other hand, the spring-summer ice debacle in the NH is primarily caused by surface ablation, which leads to a subsequent retreat of the ice cover as ice melts away at the ice edge. The decay of the Antarctic ice pack, on the contrary, is driven to a certain degree by the shortwave radiation entering the mixed layer through open water areas. This solar heat input into the upper ocean is suppressed in experiment E7; consequently, the retreat of the Antarctic ice cover is less marked than in the control simulation.

In accordance with the modeling studies of *Hibler* [1979], *Holland et al.* [1991], and *Vavrus* [1995], the total ice volume undergoes a dramatic decrease when leads are eliminated (Figures 14c and 14d). The largest decrease is observed at the time of the seasonal maximum in both hemispheres. Clearly, the reduction of bottom ablation in spring and summer is not able to offset the decrease of ice growth in autumn and winter. Figures 15a and 15b depict the changes of annual mean ice thickness in the NH and SH, respectively. Note that

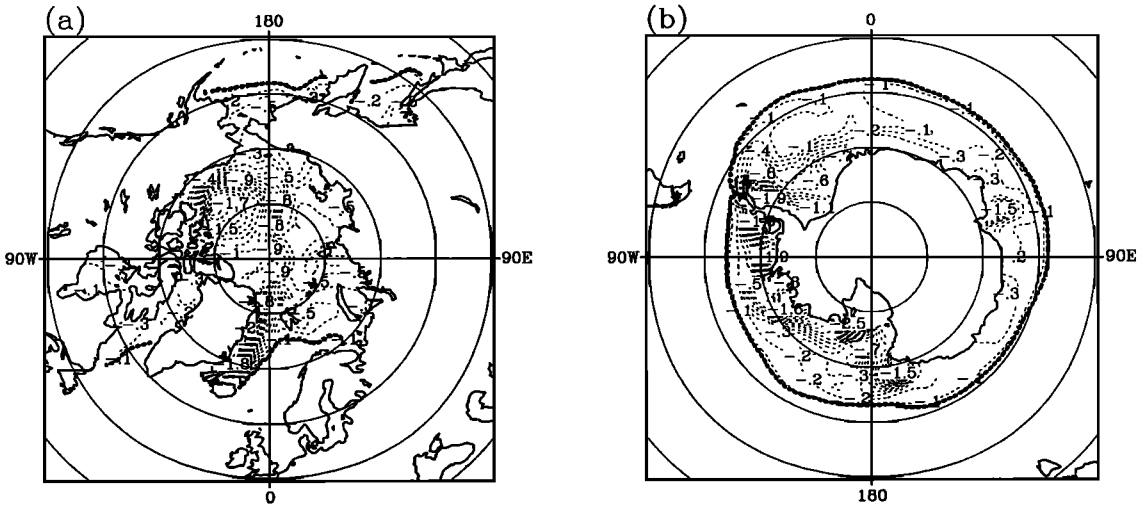

Figure 15. Geographical distribution of the difference in annual mean ice thickness between experiments E7 and E0 (a) over the Arctic Ocean and peripheral seas and (b) over the Southern Ocean. The contour interval is 0.1 m. The thick, stippled line represents the 0.1 m ice thickness contour from experiment E0.

the magnitude of the response is similar in both hemispheres; the annual mean value of $\langle h_i \rangle$ is reduced by ~0.9 m in the NH and by ~0.7 m in the SH.

As can be seen from Tables 4 and 6, the absence of leads induces drastic modifications in the simulated atmospheric and oceanic heat fluxes. Owing to the decrease in the turbulent and radiative heat losses during autumn and winter and to the reduction in the absorbed shortwave radiation during spring and summer, the amplitude of the seasonal cycle of $\langle F_{net} \rangle$ is strongly attenuated in both hemispheres. The ice being thinner, the surface temperature of the snow-ice system is noticeably higher throughout the year. However, during the fall-winter period, the replacement of leads at the freezing point by very cold, snow-covered ice yields values of $\langle T_s \rangle$ that are ~1°C lower than in experiment E0 in both hemispheres. During this period, $\langle F_{net} \rangle$ is enhanced by ~10 W m^{-2} in the NH and by ~14 W m^{-2} in the SH, on average. Roughly half of this response is ascribable to the pronounced decrease in the release of sensible heat. Between May and August (November and January), the higher albedo of the pack is responsible for a diminution in the amount of shortwave radiation absorbed at the surface that averages ~8 W m^{-2} (~21 W m^{-2}) in the NH (SH). This decrease in net shortwave radiation explains, to a great extent, the lower values taken by $\langle F_{net} \rangle$ in the course of this period. Regarding $\langle F_{wv} \rangle$, its fall and winter values are much smaller than in the control case, particularly in the marginal ice zones. This behavior is due to (1) a reduction in the net surface salt flux, which is related to the decrease in ice growth rate, and (2) a weakening of the dynamical forcing of the mixed layer, which results from the slower ice motion (the elimination of leads renders the ice much stiffer and thus more resistant to motion). In summertime, the more restricted melting leads to a reduced freshwater flux to the ocean. The upper ocean is therefore less stratified than in experiment E0 and, in consequence, $\langle F_{wv} \rangle$ takes slightly larger values.

4.3. Theme 3: Ice Dynamics

A dominant characteristic of sea ice in the polar regions is its almost constant motion and deformation. Local deformation is responsible for the appearance of open water leads whose importance has already been discussed in this paper. Ridging, another result of deformation, causes thin ice to be piled up into thick, roughly triangular features which are likely to survive the following summer melt. In addition to generating leads and pressure ridges, the ice dynamics causes advective effects which can play a pivotal role in the atmospheric and oceanic circulations. In the presence of a free ice edge, for example, advection can transfer ice to the marginal regions to be rapidly melted. The ice transport also allows net local imbalances in heat and salt to exist. An important point is that while volume transports of ice are small, the associated heat and salt transports are magnified by the latent heat of the ice and the difference in salinity between ice and seawater (about 30 practical salinity units (psu)). While the main driving forces that move sea ice come from wind and oceanic currents, the ice does not drift as a passive tracer but, rather, has a motion profoundly affected by the ice-ice interaction. The magnitude of this interaction is particularly pronounced near the coast, as manifested by the pressure ridges that often develop there. Far from shore, the effects of interaction are more subtle, but they are still considerable in that significant ice buildup is prevented by ice pressure [*Hibler*, 1989]. To quantify the relative importance of some of these features, two sensitivity experiments were performed with our model.

4.3.1. Experiment E8: Ice motion. Experiment E8 consisted of an integration of the thermody-

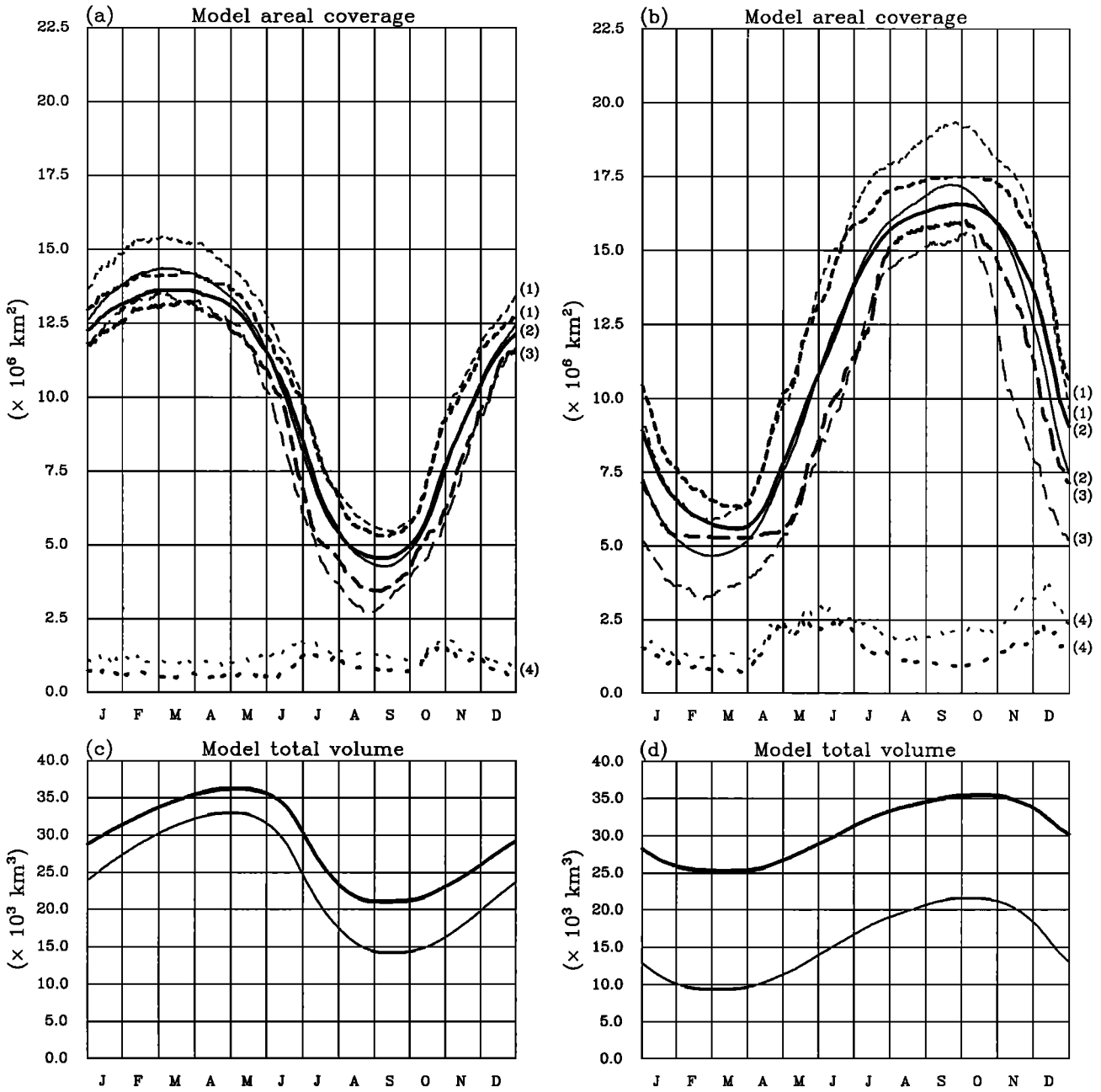

Figure 16. (a) Seasonal cycles of ice extent (curves labeled 1), effective ice area (curves labeled 2), ice area at the 85% concentration (curves labeled 3), and open water area (curves labeled 4) in the NH from experiments E8 (thick curves) and E0 (thin curves). (b) Same as Figure 16a, except for the SH. (c) Seasonal cycles of total ice volume in the NH from experiments E8 (thick curve) and E0 (thin curve). (d) Same as Figure 16c, except for the SH.

namic component of the model alone. (We stress that the uniform thickness distribution hypothesis was retained and that leads were permitted to evolve thermodynamically.) In this thermodynamics-only simulation, a prescribed spatially uniform, seasonally varying under-ice friction velocity was used. Its values for each hemisphere were derived from the control run.

The absence of ice motion has two main effects on the the simulated ice areal coverages (Figures 16a and 16b). In the first place, the seasonal variations of ice extent, effective ice area, and ice area at the 85% concentration are significantly attenuated, especially in the SH. In the second place, the amount of open water within the pack is markedly reduced (the decrease averages ~50% in winter and spring). Although the advance of the ice is primarily thermodynamic in nature, the divergent motions near the ice edge push the ice into waters which are too warm for enabling ice to form but cold enough to easily reach and stay at the freezing point when they are invaded by ice. The omission of this effect induces

a decrease in the maximum ice extent that amounts to $\sim 1.2 \times 10^6$ km^2 in the NH and to $\sim 2 \times 10^6$ km^2 in the SH. The retreat of both ice packs takes place at a somewhat slower pace when ice dynamics is eliminated. Three main reasons may be invoked to explain this behavior. First, the absence of ice transport prevents the ice near the edge from moving into warm, open waters, where it is doomed to melt. In the NH, this effect is relatively minor because of the enclosed nature of the Arctic Ocean. (During the second half of summer, the NH ice extent appears slightly smaller than in experiment E0. In fact, the ice extent is enhanced at that time over the Eurasian continental shelf but is substantially reduced in the Greenland Sea as a result of the lack of ice outflow through Fram Strait.) Second, the absence of divergent motion yields a more compact ice cover (the annual mean value of $\langle A \rangle$ is increased by ~ 0.04 in the NH and by ~ 0.07 in the SH). This enhanced compactness decreases the amount of solar energy available for melting, thereby braking the ice decay. Again, the impact is much weaker in the NH than in the SH. Third, the ice in the inner pack is generally thicker than in the control simulation and thus less inclined to melt away. An immediate consequence of the northward shift of the summer ice edge in the SH is that the retrait phase ends $2\frac{1}{2}$ weeks later than in the control case.

In both hemispheres, the total ice volume experiences an increase all year long (Figures 16c and 16d). The response is particularly dramatic in the SH, where V_i nearly doubles on an annual average. During autumn and winter, the diminution in the areas of open water and thin ice thwarts ice production. In spring and summer, ice melting is weakened, mainly because of the decrease in the amount of shortwave radiation entering the upper ocean through leads and the lack of ice advection toward the ice edge. Accordingly, the seasonal range of V_i is reduced by $\sim 3.5 \times 10^3$ km^3 in the NH and by $\sim 2 \times 10^3$ km^3 in the SH. It is noteworthy that the Antarctic ice volume has not reached a cyclostationary equilibrium at the end of the experiment, presumably because the ice basal ablation alone cannot balance the intense snow ice formation that takes place off western Antarctica. We anticipate that the largest modifications in the ice thickness field will be found in the regions of perennial ice where ice motion in experiment E0 is highly divergent or convergent. In the former regions, the ice thickness is expected to be higher since the ice created during the cold season cannot be evacuated from them. In the latter regions, the ice is expected to be thinner owing to the absence of ice buildup. The ice thickness (not shown) increases by as much as ~ 5 m in the central Arctic and by up to ~ 4 m at some places along the coastlines of the Weddell, Bellingshausen, Amundsen, and Ross Seas. Ice thins by 3 to 4 m north of the Canadian Archipelago and along the east coast of Greenland and by up to ~ 2.5 m in several coastal regions of the western sector of the Southern Ocean. In the seasonal ice zones, the ice thicknesses scarcely differ from those obtained in experiment E0. The annual mean value of $\langle h_i \rangle$ is enhanced by about 25% in the NH and by almost 100% in the SH.

In the NH, the amplitude and phase of the seasonal cycle of $\langle F_{\text{net}} \rangle$ are virtually unaltered (see Table 4). However, the winter and summer average values of this flux are ~ 8 W m^{-2} greater and ~ 5 W m^{-2} smaller, respectively, than in the control simulation. As in experiment E7, the winter increase in $\langle F_{\text{net}} \rangle$ is, for the most part, due to a decrease in the release of sensible heat. It should be noted that owing to the weaker compactness and larger thickness of the pack, $\langle T_s \rangle$ is, on average, ~ 2°C lower during winter than in experiment E0. The summer decrease in $\langle F_{\text{net}} \rangle$ arises from the fact that the reduction in lead area restricts the absorption of shortwave radiation at the surface. These explanations also apply to the SH. There, the amplitude of the seasonal cycle of $\langle F_{\text{net}} \rangle$ is decreased by 18% (see Table 6). The winter average value of $\langle F_{\text{net}} \rangle$ is ~ 8 W m^{-2} larger than in the control case, whereas the summer one is ~ 7 W m^{-2} lower. The decrease in the growth and melting rates weakens appreciably the seasonal cycle of the surface salt flux. As a result, the amplitude of the seasonal cycle of $\langle F_{wv} \rangle$ diminishes (see Tables 4 and 6). The largest changes occur during the growth season in both hemispheres. Throughout this period, $\langle F_{wv} \rangle$ is reduced by 20% to 30%. Interestingly enough, $\langle F_{wv} \rangle$ decreases noticeably during summer in the NH. The decrease in the amount of shortwave radiation transmitted through ice that follows from the thickening of the pack is mainly responsible for this behavior.

In the NH, the response of our model to the elimination of ice dynamics is comparable to that of other models [e.g., *Holland et al.*, 1991; *Flato and Hibler*, 1992]. With regard to the SH, the summer ice areal coverage exhibits a much weaker sensitivity than that reported by *Hibler and Ackley* [1983], *Hibler* [1984], *Owens and Lemke* [1990], and *Stössel et al.* [1990]. However, we emphasize that leads were absent from the standard thermodynamics-only simulations of *Hibler and Ackley* [1983] and *Hibler* [1984]. (*Owens and Lemke* [1990] and *Stössel et al.* [1990] do not mention in their papers whether leads were allowed to exist in the no-advection runs they performed.) These authors conducted additional thermodynamics-only experiments in which leads were prescribed in different ways and found a significantly reduced sensitivity. On the other hand, a feature common to the four modeling studies quoted here is that their oceanic heat flux component F_{wv} (either prescribed or diagnosed) is generally smaller in magnitude than ours. This could also account for part of the discrepancy in ice extent. *Washington et al.* [1976] and *Stössel et al.* [1990] indeed showed that the seasonal range of the Antarctic ice extent as simulated by a thermodynamics-only model increases when the oceanic heat flux is enhanced.

4.3.2. Experiment E9: Shear strength. In experiment E9, the viscous-plastic constitutive law used to compute the internal ice stress was replaced by the so-called cavitating fluid rheology (CFR). This rheology is actually a particular case of the former one and

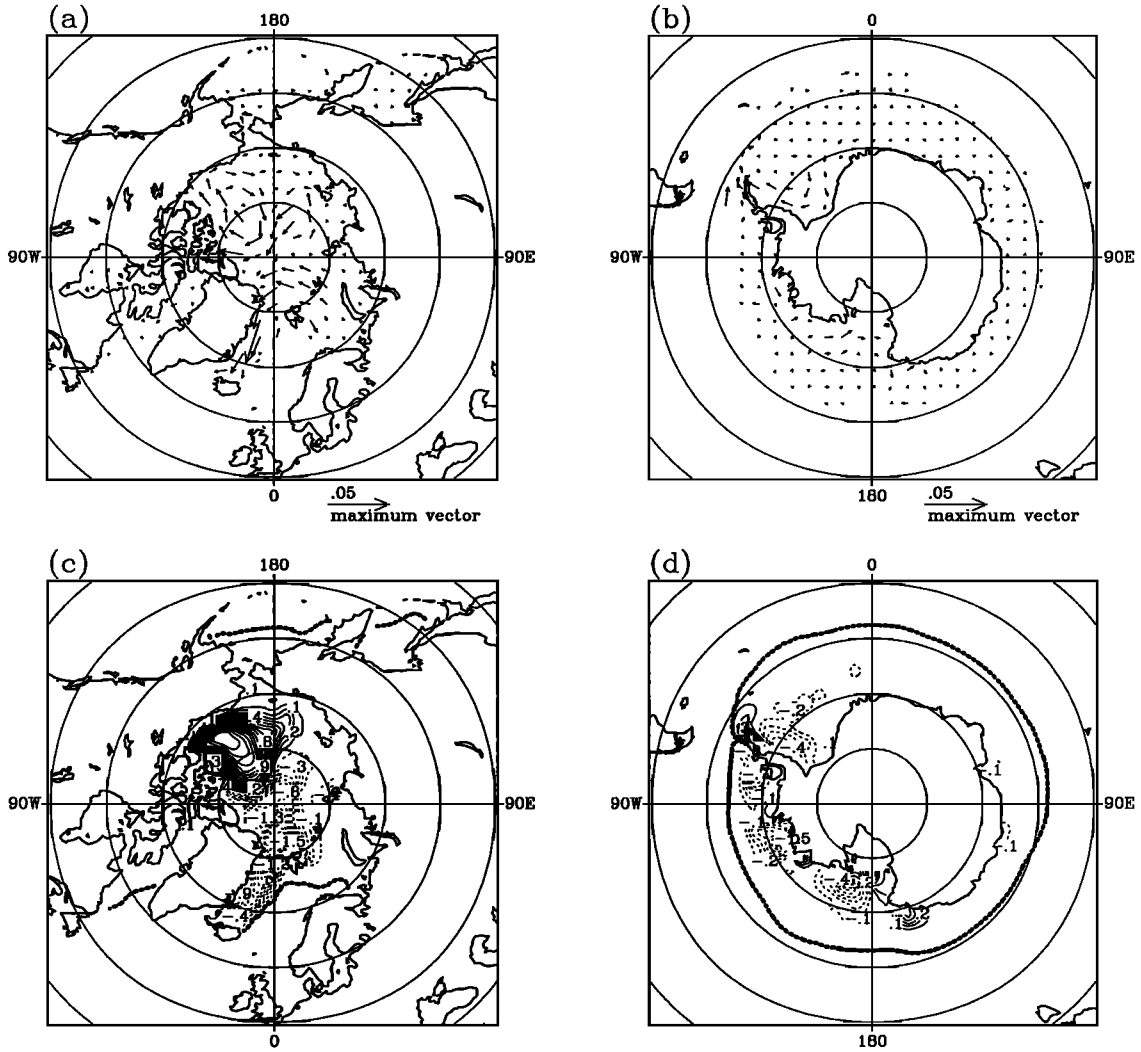

Figure 17. (a) Geographical distribution of the difference in annual mean ice velocity between experiments E9 and E0 over the Arctic Ocean and peripheral seas. The scale vector is 0.05 m s^{-1}. (b) Same as Figure 17a, except for the Southern Ocean. (c) Geographical distribution of the difference in annual mean ice thickness between experiments E9 and E0 over the Arctic Ocean and peripheral seas. The contour interval is 0.1 m. The thick, stippled line represents the 0.1 m ice thickness contour from experiment E0. (d) Same as Figure 17c, except for the Southern Ocean.

is obtained by neglecting the ice shear strength. This is easily accomplished by substituting $e_c = \infty$ in (17) and (18). *Flato and Hibler* [1992] strongly recommended using the CFR in climate studies as it is able to reproduce the most prominent features of the large-scale ice drift while being simple, computationally fast (when using a numerical scheme that turns its simplicity to account), and tolerant of long time steps. At the same time, they acknowledged that the lack of shear resistance leads to a more energetic ice pack and to somewhat different ice thickness patterns.

Tables 3 and 5 indicate that the change of rheology impacts little on the seasonal cycles of the ice areal coverage and total ice volume in both hemispheres. One notices a small decrease in ice volume throughout the year, which is more pronounced in the SH than in the NH. This decrease in V_i is primarily due to an enhanced ice transport toward the regions of strong melting located at the border of the ice pack. Another cause, albeit of secondary importance, is a weak intensification of the winter oceanic heat flux in the inner pack (see below). The slightly more vigorous ice motion induces an increase in the area of leads all year long. However, this is a very minute effect, the annual mean value of $\langle A \rangle$ being less than 0.005 smaller than the control one in both hemispheres.

Figures 17a and 17b display the changes of annual mean ice velocity in the NH and SH, respectively. In the NH, the Beaufort Gyre and the Transpolar and East Greenland Drift Streams strengthen considerably. Of particular interest is that the course of the Transpolar Drift Stream is sensibly modified. In experiment E0, this stream runs almost parallel to the Greenwich–Date Line great circle, whereas in experiment E9, it has

a significant east-west component. In the SH, where the ice drift is mainly divergent, the response is much weaker. Noticeable increases in velocity are nevertheless observed in the southwest branch of the Weddell Gyre and along the coasts of the Bellingshausen, Amundsen, and Ross Seas. In both hemispheres, the largest alterations in the ice motion take place during winter, when the wind is strong and the ice compact.

The distortions introduced in the ice velocity field by the CFR seriously affect the geographical distribution of the ice thickness in the NH. On an annual average, the ice gets thicker (by up to ~1.5 m) in the Canadian basin of the Arctic Ocean and thinner (by as much as ~1.5 m) in the Eurasian basin and in the Greenland Sea (Figure 17c). The ice accumulation that occurs in the Beaufort Gyre is easily understandable. Owing to the lack of shear stress, the tangential component of the ice velocity in the anticyclonic gyre increases. The Coriolis force is therefore enhanced, which tends to push the ice toward the interior of the gyre. As a consequence, the ice piles up around the gyre center until the internal ice stress compensates for the extra convergence. The ice that feeds this buildup is, for the most part, pumped up from the Transpolar Drift Stream. This, in turn, explains why the ice thins in the Eurasian basin. Averaged over the year, the ice outflow through Fram Strait barely diminishes. Its seasonal cycle, however, suffers profound adjustments. Between August and March, the average outflow is ~0.016 Sv weaker than in the control case, while between April and July, it is ~0.019 Sv stronger. The lessened annual importation of Arctic ice into the Greenland Sea together with the faster southward ice drift along Greenland contributes to thin the Greenland Sea ice cover. In the SH, the ice thickness field is much less disturbed. Nonetheless, decreases in annual mean ice thickness of up to ~0.5 m are encountered close to the coast in the western Weddell Sea and in the Bellingshausen, Amundsen, and Ross Seas (Figure 17d).

The seasonal cycles of $\langle F_{\mathrm{net}} \rangle$ and $\langle F_{wv} \rangle$ are nearly unchanged (see Tables 4 and 6). The only significant difference is that $\langle F_{wv} \rangle$ takes slightly larger values during the cold season (especially in the NH) as a result of the more efficient stirring of the upper ocean stimulated by the larger ice velocities.

A similar experiment was conducted by *Holland et al.* [1993] in the NH. As in our case, the ice areal coverage and total ice volume appeared quasi-insensitive to the neglect of the shear strength. By contrast, *Flato and Hibler* [1992] obtained an appreciably smaller ice volume when the viscous-plastic rheology was replaced by the CFR in their model of the Artic ice pack. They attributed this decrease in volume to the fact that the ice transport through Fram Strait underwent a strong increase in the absence of shear resistance. The sensitivity of a model, however, depends, to some degree, on the experimental conditions. The wind forcing used by *Flato and Hibler* [1992] differs substantially from the one employed in the present work; this could certainly explain part of the discrepancy in response noted here.

5. Summary and Conclusions

A global thermodynamic-dynamic sea ice model suitable for climate studies has been developed. This model has been coupled to a one-dimensional mixed layer–pycnocline model, which allows one to prognostically determine the exchange of sensible heat between ocean and sea ice. To palliate the absence of heat and salt transports by oceanic currents and deficiencies in the freshwater forcing, the temperature and salinity are restored to annual mean data at all oceanic levels. In addition to the relaxation of temperatures and salinities, the model forcing includes atmospheric fluxes of heat, freshwater, and momentum fluxes derived from monthly climatological data fields and annual mean surface geostrophic ocean currents. For the sake of consistency, a unique set of parameter values is used for both hemispheres.

The coupled model produces a reasonable simulation of the seasonal cycle of sea ice in both hemispheres. All the known major features of the seasonal evolution of ice extent, compactness, thickness, and velocity are relatively well reproduced. The model encounters, however, some problems in adequately simulating the decay phase of both ice covers. In particular, it underestimates (overestimates) the summer ice extent in the NH (SH). It also tends to generate ice packs that are slightly more compact than observed all year long. These discrepancies are partly attributable to deficiencies in the atmospheric and oceanic forcings.

The model sensitivity to the treatment of sea ice thermodynamics and dynamics has been investigated. The sea ice properties and processes we have explored are the storage of sensible and latent heat within snow and ice, the dependence of heat conduction on the subgrid-scale snow and ice thickness distributions, the presence of snow on top of sea ice and its possible transformation into snow ice, the existence of leads and polynyas within the pack, the absence of ice motion, and the ice shear strength. Each sensitivity experiment consisted of removing from the full model the parameterization of one of the processes listed above and in performing a 10-year simulation with the degraded model. While experiments targeting these different aspects of the sea ice physics have already been carried out elsewhere, our sensitivity study has the particular strength of having been conducted simultaneously for the Arctic and Antarctic environments.

The capacity of the snow-ice system to store sensible and latent heat tends to delay the spring melting and the autumnal growth of the ice cover, thus modifying the amplitude and phase of the seasonal cycle of sea ice. This effect is found to be significant in the Arctic. We have shown that it is the storage of latent heat in brine pockets which contributes mainly to the thermal inertia of the system there, the storage of sensible heat playing only a secondary role. These results lead us to state that the use of zero-layer models in numerical studies of Arctic sea ice must be avoided. Some economy in the models would, however, be achieved if the sensible heat content of ice could be disposed of. However, we

confront here a sort of dilemma in that our parameterization of the latent heat reservoir requires the determination of the ice internal temperatures. As a matter of fact, the procedure described in section 4.1.1, i.e., neglecting the storage of sensible heat and using the latent heat accumulated during summer for retarding basal ice accretion, is an excellent approach that yields results in the Arctic very close to those of the control experiment. In the SH, the influence of the thermal inertia of sea ice is rather weak owing to the relatively small thickness of the pack and to the presence of a perennial snow cover.

The ad hoc uniform thickness distribution approach that we have adopted for the computation of heat conduction has enabled us to improve the simulation of the ice growth and melting rates, especially in regions of perennial ice. This result strongly suggests that the subgrid-scale thickness distributions of snow and ice should be taken into account in sea ice models. To this effect, the most physically meaningful approach would be the inclusion in each model grid of a finite set of thickness categories which would evolve in response to thermal and mechanical forcings. Nevertheless, in cases when simplicity or computational constraints are leading considerations, the method described in this paper could be employed as poorman's alternative to the more elaborate and realistic multilevel sea ice models.

The effects of ignoring snow deposition on sea ice are comparable in both hemispheres as far as the winter ice area and volume are concerned. However, whereas the seasonal Arctic snow cover barely impacts on the decay phase of the ice cover and on the geographical distribution of ice thickness, the perennial Antarctic snow cap markedly affects the position of the summer ice edge and the ice thickness patterns in the western sector of the Southern Ocean. We have shown that the changes in the pack albedo and effective thermal conductivity that result from the removal of the snow cover seriously perturb the atmospheric and oceanic heat fluxes. It has also been demonstrated that the process of snow ice formation plays a crucial role in moderating snow accumulation in the Weddell, Bellingshausen, Amundsen, and Ross Seas.

Neglecting the presence of leads and polynyas yields a noticeable increase in the NH effective ice area. The effect is more dramatic in the SH, where the area occupied by ice increases by ~50% in summer. The slowing down of the ice growth during fall and winter causes a yearlong decrease of the ice volume in both hemispheres. Among the sensitivity experiments related to the ice thermodynamics that we have performed, the one in which leads are omitted produces the largest alterations in the atmospheric and oceanic heat fluxes. The turbulent and radiative (longwave) heat losses are strongly reduced during the cold season, while the solar energy gain undergoes a decrease of roughly comparable magnitude in spring and summer.

Some level of ice dynamics must be introduced into a sea ice model if the geographical distribution of ice thickness and the seasonal cycle of salt fluxes into the ocean are to be realistically simulated. Nevertheless, our results indicate that allowing for both a thermodynamic evolution of leads and an interactive oceanic heat flux tends to mitigate the sensitivity of the model to the absence of ice dynamics, at least with regard to the predicted ice extent and concentrations.

The cavitating fluid rheology seems to be a promising formulation for modeling sea ice dynamics in climate studies. We have shown, however, that this parameterization can introduce serious modifications in the direction and intensity of the ice drift and therefore in the ice thickness field. The ice flow is particularly sensitive to the neglect of the shear strength in regions of heavy pack ice located along the coastline, where shearing is frequently large or where the ice motion tends to be convergent.

We insist once more upon the fact that the seasonal cycle of the atmosphere and the annual state of the upper ocean circulation have been prescribed in our simulations. This precludes any feedback between the atmosphere, the sea ice, and the ocean dynamics. The real world (or even a coupled AOGCM) might respond quite differently than the constrained model used here. For instance, the albedo-temperature feedback is likely to amplify any increase or decrease in ice area encountered in our experiments. Another example is experiment E9, in which the elimination of the ice shear strength generates an ice buildup in the Beaufort Gyre. This accumulation would be probably reduced if ocean dynamics

Table 7. Importance of Sea Ice Processes in Each Hemisphere for Present-Day Climate

Process	Experiment	NH *	SH *
Storage of sensible heat	E1, E2	−	−
Storage of latent heat	E1, E2	+	−
Penetration of shortwave radiation into ice	E3	+	−
Effective heat conduction	E4	+	+
Snow cover	E5, E6	−	+
Snow ice formation	E5, E6	−	+
Leads	E7	+	+
Ice motion	E8	+	+
Shear strength	E9	?	−

Plus means important, minus means negligible, and question mark means unclear.
*NH is northern hemisphere and SH is southern hemisphere.

were included in the model. Indeed, the stronger ice-water stress would lead to an increase of the surface slope in the gyre, which would work against the ice convergence.

Our goal in this paper has been to provide climate modelers with elements of decision as to whether the sea ice properties and processes studied here are important enough to warrant their inclusion in comprehensive climate models. The results of our sensitivity analysis indicate that the behaviors of the Arctic and the Antarctic sea ice covers are very often complementary regarding their sensitivity to the processes investigated here (Table 7). In this respect, studies aimed at only one of the hemispheric ice packs could take advantage of the possible simplifications to be made in the formulation of sea ice in that hemisphere. On the other hand, each process appears to play a significant role in controlling the seasonal cycle of the ice cover in at least one of the polar oceans and therefore their omission in global climate models using a single sea ice numerical scheme seems to be barely justified.

Appendix: Use of Uniform Snow and Ice Thickness Distributions in the Computation of Heat Conduction

According to *Thorndike et al.* [1975], the subgrid-scale joint distribution of snow and ice thicknesses can be described by a probability density function $g(\xi_s, \xi_i)$, where $g(\xi_s, \xi_i)\, d\xi_s d\xi_i$ is the fraction of area (in a given region) occupied by snow and ice with thicknesses ranging from ξ_s to $\xi_s + d\xi_s$ and from ξ_i to $\xi_i + d\xi_i$, respectively. If we assume that the snow depressed below sea level transforms into ice, then $g(\xi_s, \xi_i)$ is zero for $\xi_s > [(\rho_w - \rho_i)/\rho_s]\,\xi_i$, where ρ_s, ρ_i, and ρ_w are the densities of snow, ice, and seawater, respectively. If open water exists within the pack, $g(\xi_s, \xi_i)$ has a singularity at $\xi_i = 0$. To isolate this singularity, we can rewrite the probability density function as $g(\xi_s, \xi_i) = (1 - A)\,\delta(\xi_i) + A\, g^+(\xi_s, \xi_i)$, where A is the ice concentration, $\delta(\xi_i)$ is the Dirac delta function, and $g^+(\xi_s, \xi_i)$, which is defined only for $\xi_i > 0$, is such that $\int_{0+}^{\infty} d\xi_i \int_0^{\infty} g^+(\xi_s, \xi_i)\, d\xi_s = 1$. Suppose now that the ice thickness is uniformly distributed between zero and twice its mean value over the oceanic area covered by ice and that the ratio of snow depth to ice thickness is the same for all ice thicknesses. In this case, one has

$$g^+(\xi_s, \xi_i) = \begin{cases} \delta(\xi_s - \frac{h_s}{h_i}\xi_i)\,\frac{1}{2h_i} & 0 < \xi_i \le 2\,h_i \\ 0 & \xi_i > 2\,h_i \end{cases} \tag{A1}$$

where h_s and h_i are the mean thicknesses of snow and ice over the oceanic area covered by ice, respectively.

The statistical properties of any (ξ_s, ξ_i)-dependent variable can be derived from the probability density function $g(\xi_s, \xi_i)$. Let us consider the case of the internal conductive heat flux Γ_c. Ignoring the heat capacity of the snow-ice system system, this heat flux can be written as (see, for example, *Semtner* [1976])

$$\Gamma_c = -\frac{k_e}{\xi_e}\,(T_{su} - T_b) \tag{A2}$$

where $k_e = (k_s k_i)/(k_s + k_i)$ is an effective thermal conductivity (k_s and k_i are the thermal conductivities of snow and ice, respectively), $\xi_e = k_e(\xi_s/k_s + \xi_i/k_i)$ is the effective thickness of the snow-ice system, T_{su}, which depends on ξ_e, is the top snow or ice temperature, and T_b is the temperature at the ice bottom. The distribution of ξ_e can be described by a probability density function $g_e(\xi_e)$, which is related to $g(\xi_s, \xi_i)$ by

$$g_e(\xi_e) = \int_{-\infty}^{+\infty} \frac{(k_s + k_i)^2}{k_s^2 + k_i^2}\, g\left[\xi_s(\xi_e, \chi_e), \xi_i(\xi_e, \chi_e)\right] d\chi_e \tag{A3}$$

where $\chi_e = k_e(\xi_s/k_i - \xi_i/k_s)$. Like $g(\xi_s, \xi_i)$, $g_e(\xi_e)$ is made of two components, a delta component at $\xi_e = 0$ and a contribution from the ice-covered area, namely, $g_e^+(\xi_e)$. The mean effective thickness is simply given by $h_e = \int_{0+}^{\infty} \xi_e\, g_e^+(\xi_e)\, d\xi_e$. As shown later on, under horizontally homogeneous atmospheric and oceanic forcing conditions, T_{su} is nearly the same for all thickness categories, provided that the effective thicknesses are larger than a certain threshold ϵ. Thus if we assume that in the thickness range $0 \le \xi_e \le \epsilon$, T_{su} varies linearly with ξ_e between T_b and T_{su}^*, the surface temperature of thick snow/ice ($\xi_e > \epsilon$), the average conductive heat flux F_c is

$$F_c = -k_e\,(T_{su}^* - T_b)\left[\frac{1}{\epsilon}\int_{0+}^{\epsilon} g_e^+(\xi_e)\, d\xi_e + \int_{\epsilon}^{\infty} \frac{1}{\xi_e}\, g_e^+(\xi_e)\, d\xi_e\right] \tag{A4}$$

We now define a conduction correction factor $G(h_e)$ such that $F_c = -G(h_e)\, k_e\,(T_{su}^* - T_b)/h_e$. Equation (A4) implies that $G(h_e)$ has the form

$$G(h_e) = h_e\left[\frac{1}{\epsilon}\int_{0+}^{\epsilon} g_e^+(\xi_e)\, d\xi_e + \int_{\epsilon}^{\infty} \frac{1}{\xi_e}\, g_e^+(\xi_e)\, d\xi_e\right] \tag{A5}$$

This factor can be explicitly computed if the thickness distribution $g_e^+(\xi_e)$ is known. In the case of a uniform thickness distribution, $G(h_e)$ is readily obtained as

$$G(h_e) = 1 + \frac{1}{2}\ln\left(\frac{2h_e}{e\epsilon}\right) \tag{A6}$$

where e is the base of the natural logarithms and $h_e = [(k_s k_i)/(k_s + k_i)]\,(h_s/k_s + h_i/k_i)$. It should be noted that for $h_e < e\epsilon/2$, $G(h_e)$ has to be taken equal to 1.

The problem remains of setting a suitable value for the threshold thickness ϵ. This threshold thickness marks the point beyond which variations in the effective thickness barely affect the surface temperature. T_{su} is obtained from the surface heat balance equation,

$$(1-i_0)(1-\alpha_{su})\Gamma_{sw}+\varepsilon_{su}\Gamma_{lw}-\varepsilon_{su}\sigma T_{su}^4 +\Gamma_h+\Gamma_{le}+\Gamma_c=0 \qquad \text{(A7)}$$

where Γ_{sw} is the incoming shortwave radiation, α_{su} is the surface albedo, i_0 is the fraction of the net shortwave radiation that penetrates the snow or bare ice, Γ_{lw} is the incoming longwave radiation, ε_{su} is the surface emissivity, σ is the Stefan-Boltzmann constant, and Γ_h and Γ_{le} are the turbulent fluxes of sensible heat and latent heat, respectively. The outgoing longwave radiation and the sensible and latent heat fluxes all three depend on ξ_e through T_{su}. (The first term on the left-hand side of (A7) also depends on ξ_e because α_{su} is a function of both ξ_e and T_{su}, but we ignore this dependence in our present analysis. During the period of surface melting, when this term takes its largest values, the surface temperature is kept fixed to the melting point and, consequently, it is independent of ξ_e.) The derivation of (A7) with respect to ξ_e leads to

$$\frac{dT_{su}/d\xi_e}{(T_{su}-T_b)/\xi_e}=\frac{k_e/\xi_e}{K(T_{su})+k_e/\xi_e} \qquad \text{(A8)}$$

where $K(T_{su})=\varepsilon_{su}\sigma 4T_{su}^3-d(\Gamma_h+\Gamma_{le})/dT_{su}$. $K(T_{su})$ ranges from $\sim$28 W m^{-2} K^{-1} for $T_{su}=0$°C to $\sim$27 W m^{-2} K^{-1} for $T_{su}=-40$°C. It can therefore be considered as a constant. Under this assumption, the solution of (A8) is

$$T_{su}-T_b=(T_{su}^*-T_b)\left(\frac{K+k_e/\epsilon}{K+k_e/\xi_e}\right) \qquad \text{(A9)}$$

From this, it is easy to verify that T_{su} changes by less than about 10% of $(T_{su}^*-T_b)$ for $\xi_e \geq \epsilon \geq 0.1$ m. Thus we set $\epsilon = 0.1$ m. For bare ice, this threshold thickness corresponds to an actual ice thickness of 0.75 m. For ice supporting a maximum snow load (just before an episode of snow ice formation), the corresponding thickness is 0.2 m.

The original formulation of the correction factor $G(h_e)$ is due to *Mellor and Kantha* [1989]. *Häkkinen and Mellor* [1990] applied it in a one-dimensional simulation of the Arctic ice pack. However, $G(h_e)$ was, in their models, an external parameter whose value was empirically determined from observed thickness distribution functions. It was temporally and spatially constant and did not take into account the effect of snow on top of sea ice. On the other hand, in our formulation, which owes much to the approach of these authors, $G(h_e)$ is an internally diagnosed parameter that varies in both time and space, adopts significantly different values in the NH and SH, and incorporates the contribution of snow to the effective heat conductivity.

Although quite simple, the parameterization described above allows one to take into account the first-order effect of the existence of subgrid-scale snow and ice thickness distributions on the average heat conduction. For the mean snow and ice thicknesses that prevail in the central Arctic during wintertime (i.e., 0.3 and 3 m, respectively), $G(h_e)=1.8$. This value is not far from the estimate made by *Mellor and Kantha* [1989] from observed ice thickness distribution functions in the central Arctic. In winter, the average thickness of the Antarctic ice pack is $\sim$1 m and the mean snow depth amounts to $\sim$0.3 m. For these values, $G(h_e)=1.5$.

Acknowledgments. We thank H. Goosse, W. Hibler, D. Holland, D. Martinson, L. Mysak, R. Preller, S. Planton, and A. Stössel for helpful discussions about various aspects of this work. We also thank J. Backhaus and two anonymous referees for their careful reading of the manuscript and constructive criticism. C. Hanson and M. Holm from NSIDC kindly provided us with the SMMR ice concentration data. T. Fichefet is a Research Associate at the National Fund for Scientific Research (Belgium). This work was done within the scope of the Impulse Programme Global Change (Belgian State, Prime Minister's Services, Federal Office for Scientific, Technical, and Cultural Affairs, contract GC/10/013), the Concerted Research Action 092/97-154 (French Community of Belgium, Department of Education, Research, and Formation), the Environment and Climate Programme (European Commission, contract ENV4-CT95-0102), and a study contract with Digital Europe (external research agreement, contract BE-011). All of this support is gratefully acknowledged.

References

Aagaard, K. L., and P. Greisman, Toward new mass and heat budgets for the Arctic Ocean, *J. Geophys. Res.*, *80*, 3821–3827, 1975.

Allison, I., Antarctic sea ice growth and oceanic heat flux, in *Sea Level, Ice, and Climatic Change*, edited by I. Allison, *IAHS Publ. 131*, 161–170, 1981.

Allison, I., Pack-ice drift off East Antarctica and some implications, *Ann. Glaciol.*, *12*, 1–8, 1989.

Andreas, E. L., and S. F. Ackley, On the differences in ablation seasons of the Arctic and Antarctic sea ice, *J. Atmos. Sci.*, *39*, 440–447, 1982.

Arakawa, A., Computational design of long-term numerical integration of the equations of fluid motion, *J. Comput. Phys.*, *1*, 119–143, 1966.

Berliand M. E., and T. G. Strokina, *Global Distribution of the Total Amount of Clouds* (in Russian), 71 pp., Hydrometeorological, Leningrad, Russia, 1980.

Bourke, R. H., and R. P. Garrett, Sea ice thickness distribution in the Arctic Ocean, *Cold Reg. Sci. Technol.*, *13*, 259–280, 1987.

Budd, W. F., Antarctica and global change, *Clim. Change*, *18*, 272–299, 1991.

Cavalieri, D. J., The validation of geophysical products using multisensor data, in *Microwave Remote Sensing of Sea ice, Geophys. Monogr. Ser.*, vol. 68, edited by F. D. Carsey, pp. 233–242, AGU, Washington, D. C., 1992.

Colony, R., and A. S. Thorndike, An estimate of the mean field of Arctic sea ice motion, *J. Geophys. Res.*, *89*, 10,623–10,629, 1984.

Comiso, J. C., and A. L. Gordon, Recurring polynyas over the Cosmonaut Sea and the Maud Rise, *J. Geophys. Res.*, *92*, 2819–2833, 1987.

Crutcher, H. L., and J. M. Meserve, Selected level heights, temperatures and dew points for the Northern Hemisphere, *NAVAIR Rep. 50-1C-52*, revised, U. S. Nav. Weather Serv. Command, Washington, D. C., 1970.

Cubasch, U., K. Hasselmann, H. Höck, E. Maier-Reimer, U. Mikolajewicz, B. D. Santer, and R. Sausen, Time-dependent greenhouse warming computations with a cou-

pled ocean-atmosphere model, *Clim. Dyn.*, *8*, 55–69, 1992.

Curry, J. A., J. L. Schramm, and E. E. Ebert, Sea ice–albedo climate feedback mechanism, *J. Clim.*, *8*, 240–247, 1995.

Doronin, Y. P., and D. E. Kheisin, *Sea Ice*, 323 pp., Amerind, New Delhi, India, 1977.

Ebert, E. E., and J. A. Curry, An intermediate one-dimensional thermodynamic sea ice model for investigating ice-atmosphere interactions, *J. Geophys. Res.*, *98*, 10,085–10,109, 1993.

Eicken, H., M. A. Lange, H.-W. Hubberten, and P. Wadhams, Characteristics and distribution patterns of snow and meteoric ice in the Weddell Sea and their contribution to the mass balance of sea ice, *Ann. Geophys.*, *12*, 80–93, 1994.

Eicken, H., H. Fischer, and P. Lemke, Effects of snow cover on Antarctic sea ice and potential modulation of its response to climate change, *Ann. Glaciol.*, *21*, 369–376, 1995.

Englebretson, R. E., and J. E. Walsh, Fram Strait ice flux calculations and associated Arctic ice conditions, *GeoJournal*, *18*, 61–67, 1989.

Fichefet, T., and P. Gaspar, A model study of upper ocean–sea ice interactions, *J. Phys. Oceanogr.*, *18*, 181–195, 1988.

Flato, G. M., and W. D. Hibler III, Modelling pack ice as a cavitating fluid, *J. Phys. Oceanogr.*, *22*, 626–651, 1992.

Flato, G. M., and W. D. Hibler III, Ridging and strength in modeling the thickness distribution of Arctic sea ice, *J. Geophys. Res.*, *100*, 18,611–18,626, 1995.

Gaspar, P., Modeling the seasonal cycle of the upper ocean, *J. Phys. Oceanogr.*, *18*, 161–180, 1988.

Gloersen, P., W. J. Campbell, D. J. Cavalieri, J. C. Comiso, C. L. Parkinson, and H. J. Zwally, Arctic and Antarctic sea ice, 1978–1987: Satellite passive-microwave observations and analysis, *NASA Spec. Publ.*, *SP-511*, 290 pp., 1992.

Gordon, A. L., and B. A. Huber, Southern Ocean winter mixed layer, *J. Geophys. Res.*, *95*, 11,655–11,672, 1990.

Grenfell, T. C., and G. A. Maykut, The optical properties of ice and snow in the Arctic basin, *J. Glaciol.*, *18*, 445–463, 1977.

Häkkinen, S., and G. L. Mellor, One hundred years of Arctic ice cover variations as simulated by a one-dimensional, ice-ocean model, *J. Geophys. Res.*, *95*, 15,959–15,969, 1990.

Häkkinen, S., and G. L. Mellor, Modeling the seasonal variability of a coupled Arctic ice-ocean system, *J. Geophys. Res.*, *97*, 20,285–20,304, 1992.

Harvey, L. D. D., Development of a sea ice model for use in zonally averaged energy balance climate models, *J. Clim.*, *1*, 1221–1238, 1988.

Hibler, W. D., III, A dynamic thermodynamic sea ice model, *J. Phys. Oceanogr.*, *9*, 815–846, 1979.

Hibler, W. D., III, Modeling a variable thickness sea ice cover, *Mon. Weather Rev.*, *108*, 1943–1973, 1980.

Hibler, W. D., III, The role of sea ice dynamics in modeling CO_2 increases, in *Climate Processes and Climate Sensitivity, Geophys. Monogr. Ser.*, vol. 29, edited by J. E. Hansen and T. Takahashi, pp. 238–253, AGU, Washington, D. C., 1984.

Hibler, W. D., III, Arctic ice-ocean dynamics, in *The Arctic Seas*, edited by Y. Herman, pp. 47–91, Van Nostrand Reinhold, New York, 1989.

Hibler, W. D., III, The role of sea ice dynamics in global climate change, in *Modeling the Earth System*, edited by D. Ojima, pp. 107–129, Off. for Interdisciplinary Earth Stud., Univ. Corp. for Atmos. Res., Boulder, Colo., 1992.

Hibler, W. D., III, and S. F. Ackley, Numerical simulation of the Weddell Sea pack ice, *J. Geophys. Res.*, *88*, 2873–2887, 1983.

Holland, D. M., L. A. Mysak, and J. M. Oberhuber, Sensitivity study of a dynamic thermodynamic sea ice model, *Res. Rep. 91-22*, 400 pp., Cent. for Clim. and Global Change Res., McGill Univ., Montreal, Que., 1991.

Holland, D. M., L. A. Mysak, D. K. Manak, and J. M. Oberhuber, Sensitivity study of a dynamic thermodynamic sea ice model, *J. Geophys. Res.*, *98*, 2561–2586, 1993.

Jacobs, S. S., and J. C. Comiso, Sea ice and oceanic processes on the Ross Sea continental shelf, *J. Geophys. Res.*, *94*, 18,195–18,211, 1989.

Jaeger, L., Monatskarten des niederschlags für die ganze Erde, *Ber. Dtsch. Wetterdienstes*, *139*, 38 pp., 1976.

Jeffries, M. O., R. A. Shaw, K. Morris, A. L. Veazey, and H. R. Krouse, Crystal structure, stable isotopes ($\delta^{18}O$), and development of sea ice in the Ross, Amundsen, and Bellingshausen seas, Antarctica, *J. Geophys. Res.*, *99*, 985–995, 1994.

Jerlov, N. G., *Marine Optics, Elsevier Oceanogr. Ser.*, vol. 14, 231 pp., Elsevier, New York, 1976.

Kottmeier, C., J. Olf, W. Frieden, and R. Roth, Wind forcing and ice motion in the Weddell Sea region, *J. Geophys. Res.*, *97*, 20,373–20,383, 1992.

Lange, M. A., P. Schlosser, S. F. Ackley, P. Wadhams, and G. S. Dieckmann, ^{18}O concentrations in sea ice of the Weddell Sea, Antarctica, *J. Glaciol.*, *36*, 315–323, 1990.

Ledley, T. S., Sensitivity of a thermodynamic sea ice model with leads to time step size, *J. Geophys. Res.*, *90*, 2251–2260, 1985.

Ledley, T. S., Snow on sea ice: Competing effects in shaping climate, *J. Geophys. Res.*, *96*, 17,195–17,208, 1991.

Ledley, T. S., Variations in snow on sea ice: A mechanism for producing climate variations, *J. Geophys. Res.*, *98*, 10,401–10,410, 1993.

Lemke, P., W. B. Owens, and W. D. Hibler III, A coupled sea ice–mixed layer–pycnocline model for the Weddell Sea, *J. Geophys. Res.*, *95*, 9513–9525, 1990.

Levitus, S., Climatological atlas of the world ocean, *NOAA Prof. Pap. 13*, 173 pp., U. S. Gov. Print. Office, Washington, D. C., 1982.

Lunkeit, F., R. Sausen, and J. M. Oberhuber, Climate simulations with the global coupled atmosphere-ocean model ECHAM2/OPYC, *Clim. Dyn.*, *12*, 195–212, 1996.

Manabe, S., R. J. Stouffer, M. J. Spelman, and K. Bryan, Transient responses of a coupled ocean-atmosphere model to gradual changes of atmospheric CO_2, I, Annual mean response, *J. Clim.*, *4*, 785–818, 1991.

Marotzke, J., Influence of convective adjustment on the stability of the thermohaline circulation, *J. Phys. Oceanogr.*, *21*, 903–907, 1991.

Martinson, D. G., Ocean heat and seasonal sea ice thickness in the Southern Ocean, in *Ice in the Climate System, NATO ASI Ser., Ser. I*, vol. 12, edited by W. R. Peltier, pp. 597–609, Springer-Verlag, New York, 1993.

Maykut, G. A., Large-scale heat exchange and ice production in the central Arctic, *J. Geophys. Res.*, *87*, 7971–7984, 1982.

Maykut, G. A., and M. G. McPhee, Solar heating of the Arctic mixed layer, *J. Geophys. Res.*, *100*, 24,691–24,703, 1995.

Maykut, G. A., and D. K. Perovich, The role of shortwave radiation in the summer decay of a sea ice cover, *J. Geophys. Res.*, *92*, 7032–7044, 1987.

Maykut, G. A., and N. Untersteiner, Some results from a time-dependent thermodynamic model of sea ice, *J. Geophys. Res.*, *76*, 1550–1575, 1971.

McPhee, M. G., and N. Untersteiner, Using sea ice to measure heat flux in the ocean, *J. Geophys. Res.*, *87*, 2071–2074, 1982.

Meehl, G. A., W. M. Washington, and T. R. Karl, Low-

frequency variability and CO_2 transient climate change, I, Time-averaged differences, *Clim. Dyn.*, *8*, 117–133, 1993.

Mellor, G. L., and L. Kantha, An ice-ocean coupled model, *J. Geophys. Res.*, *94*, 10,937–10,954, 1989.

Murphy, J. M., and J. F. B. Mitchell, Transient response of the Hadley Centre coupled ocean-atmosphere model to increasing carbon dioxide, II, Spatial and temporal structure of response, *J. Clim.*, *8*, 57–80, 1995.

Overland, J. E., and R. L. Colony, Geostrophic drag coefficients for the central Arctic derived from Soviet drifting station data, *Tellus, Ser. A*, *46*, 75–85, 1994.

Overland, J. E., and C. H. Pease, Modeling ice dynamics of coastal seas, *J. Geophys. Res.*, *93*, 15,619–15,637, 1988.

Owens, W. B., and P. Lemke, Sensitivity studies with a sea ice–mixed layer–pycnocline model in the Weddell Sea, *J. Geophys. Res.*, *95*, 9527–9538, 1990.

Paulson, C. A., and J. Simpson, Irradiance measurements in the upper ocean, *J. Phys. Oceanogr.*, *7*, 952–956, 1977.

Peggion, G., A method for determining absolute velocities from hydrographic data, *Rep. SR-114*, 28 pp., SACLANT Res. Cent., La Spezia, Italy, 1987.

Perovich, D. K., and G. A. Maykut, Solar heating of a stratified ocean in the presence of a static ice cover, *J. Geophys. Res.*, *95*, 18,233–18,245, 1990.

Pollard, D., and S. L. Thompson, Sea-ice dynamics and CO_2 sensitivity in a global climate model, *Atmos. Ocean*, *32*, 449–467, 1994.

Prather, M. C., Numerical advection by conservation of second-order moments, *J. Geophys. Res.*, *91*, 6671–6681, 1986.

Semtner, A. J., Jr., A model for the thermodynamic growth of sea ice in numerical investigations of climate, *J. Phys. Oceanogr.*, *6*, 379–389, 1976.

Semtner, A. J., Jr., On modelling the seasonal thermodynamic cycle of sea ice in studies of climatic change, *Clim. Change*, *6*, 27–37, 1984.

Simonot, J.-Y., and H. Le Treut, A climatological field of mean optical properties of the world ocean, *J. Geophys. Res.*, *91*, 6642–6646, 1986.

Snyder, J. P., and P. M. Voxland, An album of map projections, *U. S. Geol. Surv. Prof. Pap. 1453*, 249 pp., 1989.

Steele, M., Sea ice melting and floe geometry in a simple ice-ocean model, *J. Geophys. Res.*, *97*, 17,729–17,738, 1992.

Steffen, K., J. Key, D. J. Cavalieri, J. Comiso, P. Gloersen, K. St. Germain, and I. Rubinstein, The estimation of geophysical parameters using passive microwave algorithms, in *Microwave Remote Sensing of Sea Ice, Geophys. Monogr. Ser.*, vol. 68, edited by F. D. Carsey, pp. 201–231, AGU, Washington, D. C., 1992.

Stern, H. L., and D. A. Rothrock, Open water production in Arctic sea ice: Satellite measurements and model parameterizations, *J. Geophys. Res.*, *100*, 20,601–20,612, 1995.

Stössel, A., P. Lemke, and W. B. Owens, Coupled sea ice–mixed layer simulations for the Southern Ocean, *J. Geophys. Res.*, *95*, 9539–9555, 1990.

Taljaard, J. J., H. van Loon, H. L. Crutcher, and R. L. Jenne, Climate of the upper air, I, Southern Hemisphere, vol. 1, Temperatures, dew points, and heights at selected pressure levels, *NAVAIR Rep. 50-1C-55*, 135 pp., U. S. Nav. Weather Serv. Command, Washington, D. C., 1969.

The Polar Group, Polar atmosphere-ice-ocean processes: A review of polar problems in climate research, *Rev. Geophys.*, *18*, 525–543, 1980.

Thorndike, A. S., Kinematics of sea ice, in *The Geophysics of Sea Ice, NATO ASI Ser., Ser. B*, vol. 146, edited by N. Untersteiner, pp. 489–549, Plenum, New York, 1986a.

Thorndike, A. S., Diffusion of sea ice, *J. Geophys. Res.*, *91*, 7691–7696, 1986b.

Thorndike, A. S., D. A. Rothrock, G. A. Maykut, and R. Colony, The thickness distribution of sea ice, *J. Geophys. Res.*, *80*, 4501–4513, 1975.

Vavrus, S. J., Sensitivity of the Arctic climate to leads in a coupled atmosphere–mixed layer ocean model, *J. Clim.*, *8*, 158–171, 1995.

Washington, W. M., A. J. Semtner Jr., C. Parkinson, and L. Morrison, On the development of a seasonal change sea-ice model, *J. Phys. Oceanogr.*, *6*, 679–685, 1976.

Wettlaufer, J. S., Heat flux at the ice-ocean interface, *J. Geophys. Res.*, *96*, 7215–7236, 1991.

World Meteorological Organization, Organization of an International Programme for Antarctic Buoys, summary report, Launching Meeting on a WCRP International Programme for Antarctic Buoys (Helsinki, Finland, 20-22 June 1994), Geneva, 1994.

Zwally, H. J., J. C. Comiso, and A. L. Gordon, Antarctic offshore leads and polynyas and oceanographic effects, in *Oceanology of the Antarctic Continental Shelf, Antarc. Res. Ser.*, vol. 43, edited by S. Jacobs, pp. 203–226, AGU, Washington, D. C., 1985.

T. Fichefet, Institut d'Astronomie et de Géophysique G. Lemaître, Université Catholique de Louvain, Louvain-la-Neuve, B-1348, Belgium. (e-mail: fichefet@astr.ucl.ac.be)

M. A. Morales Maqueda, Department of Mathematics, University of Keele, Keele, Staffordshire, ST5 5BG, England. (e-mail: maa21@cc.keele.ac.uk)

(Received July 8, 1996; revised January 27, 1997; accepted January 31, 1997.)